NASA Dragonfly Mission – Coaxial Rotor Test & CFD Prediction

Sven Schmitz
Boeing/A.D. Welliver Professor
Dept. of Aerospace Engineering
Penn State University
University Park, PA 16802

Jason Cornelius
Aerospace Engineer
Aeromechanics Office
NASA Ames Research Center
Moffet Field, CA 94035

Gracelyne Allred
Graduate Student Researcher
Dept. of Aerospace Engineering
Penn State University
University Park, PA 16802

Jose Palacios
Associate Professor
Dept. of Aerospace Engineering
Penn State University
University Park, PA 16802

Richard R. Heisler
Principal Professional Staff
Johns Hopkins University
Applied Physics Laboratory
Laurel, MD 20723-6099

Bernadine Juliano
Senior Professional Staff
Johns Hopkins University
Applied Physics Laboratory
Laurel, MD 20723-6099

Gino Perrotta
Senior Professional Staff
Johns Hopkins University
Applied Physics Laboratory
Laurel, MD 20723-6099

Felipe Ruiz
Senior Professional Staff
Johns Hopkins University
Applied Physics Laboratory
Laurel, MD 20723-6099

ABSTRACT

A fixed-pitch speed-controlled coaxial rotor system (Dragonfly Phase B*) was tested in the NASA Langley Transonic Dynamics Tunnel (TDT). The rotors have a diameter (D) of 1.35 meters and an inter-rotor spacing of 0.3375 meters, or D/4. The primary objective of the TDT test was to experimentally measure rotor performance of a candidate full-scale flight rotor for the Dragonfly program, NASA's 4th New Frontiers Mission, in an atmosphere as close as possible to that on Saturn's largest moon Titan. The TDT heavy gas (HG) test setup provided Mach scaled data at one-third chord-based Reynolds number when compared to Titan condition. These data serve as a validation anchor for computational fluid dynamics (CFD) performance tables used by the Dragonfly team to predict rotor performance on Titan. The present work provides a thorough CFD validation study of coaxial rotor performance estimation with accuracy of order 5-10% over the primary flight envelope using an efficient hybrid BEMT-URANS flow solver, RotCFD. Airfoil lookup tables (i.e. C81 tables) were generated in OVERFLOW, run fully-turbulent using the Spalart-Allmaras turbulence model. The full CFD performance matrix consisted of more than 1,500 cases total, including hover, climb, edgewise flight, descent, vortex ring state (VRS), turbulent wake state (TWS), and windmill brake state (WBS). Significant effort was devoted to quantitative comparisons between experimental data and CFD results, with emphasis on uncertainty quantification and confidence levels of performance predictions. This work has been instrumental in establishing the hybrid BEMT-URANS methodology to provide mean coaxial rotor performance data for Dragonfly Mobility Closed-Loop Simulations.

NOTATION

AOA	Angle of Attack [deg]
A	Rotor Swept Disk Area [m^2]
a	Speed of Sound [m/s]
c_d	Sectional Drag Coefficient
c_l	Sectional Lift Coefficient
C_T	Rotor Thrust Coefficient, $T/(\rho A V_{Tip}^2)$
C_Q	Rotor Torque Coefficient, $T/(\rho A V_{Tip}^2 R)$
c_r	Chord Length at Radial Position, r [m]
D	Rotor Diameter [m]
FM	Figure of Merit, $\frac{T^{3/2}}{\sqrt{2}\rho\Omega}$
N_b	Number of Rotor Blades
P	Rotor Power [W]
Ma	Freestream Mach Number, V_∞/a
Ma_r	Local Mach Number, $\Omega\omega\, r/a$
Re	Local Reynolds Number, $\rho\Omega r c_r/\nu$
R	Rotor Blade Radius [m]
r	Radial Position Along Blade [m]
SA	Shaft Angle, between free-stream and rotor disk
T	Rotor Thrust [N]
Q	Rotor Torque [N-m]
V	Wind Tunnel Speed [m/s]
V_{Tip}	Blade Tip Speed, ΩR [m/s]
V_x	Rotor Edgewise (Forward) Speed, $V * \cos(SA)$
V_z	Rotor Axial (Vertical) Speed, $-V * \sin(SA)$ $[m/s]$
v_h	Equivalent Hover Induced Velocity $\sqrt{\frac{T}{2\rho A}}$ [m/s]
x, y, z	Cartesian Coordinate System [m]
ρ	Density [kg/m^3]
ν	Kinematic Viscosity [m^2/s]

Presented at the Vertical Flight Society's 81st Annual Forum & Technology Display, Virginia Beach, VA, USA, May 20-22, 2025.

Ω	Rotor Rotational Velocity [rad/s]
μ, J	Rotor Advance Ratio, $V_\infty / (\Omega R)$
μ_x	Rotor Advance Ratio Parallel to Rotor Disk, $(\cos(SA) * V_\infty) / (\Omega R)$
u	Uncertainty [non-dimensional]
δ	Error [non-dimensional]

ACRONYMS

3D	Three-Dimensional
BEMT	Blade Element Momentum Theory
CAD	Computer Aided Design
CFD	Computational Fluid Dynamics
CLS	Closed-Loop Simulation
CPU	Central Processing Unit
DAQ	Data Acquisition System
ESC	Electronic Speed Controller
EXP	Experimental (TDT Data)
GPU	Graphics Processing Unit
HG	Heavy Gas (i.e. R-134a in TDT facility)
k-ε	K-Epsilon Turbulence Model
NACA	National Advisory Committee for Aeronautics
NASA	National Aeronautics and Space Administration
PPF	Preparation for Powered Flight
RPM	Revolutions per Minute
RotCFD	Rotorcraft Computational Fluid Dynamics
TDT	Transonic Dynamics Tunnel
TPF	Transition to Powered Flight
TWS	Turbulent Wake State
UAS	Unmanned Aerial Systems
URANS	Unsteady Reynolds-averaged Navier-Stokes
VRS	Vortex Ring State
WBS	Windmill Brake State

INTRODUCTION

In 1655, Saturn's largest moon Titan was discovered by Dutch astronomer Christian Huygens. It was not until the Voyager flybys of 1980-1981 that Titan was identified as one of the most interesting planetary bodies in the solar system. In fact, Titan holds a thick nitrogen atmosphere with a liquid methane cycle at about 14% Earth gravity and is for many reasons a candidate for signs of pre-biotic organic chemistry on its surface, Ref. 1. In early 2005, the Cassini-Huygens probe photographed the surface of Titan. Furthermore, Cassini data have been used to create composite maps of Titan's surface. In 2019, NASA awarded the 4th New Frontiers mission to the Johns Hopkins University Applied Physics Laboratory (JHUAPL) to send a rotorcraft the size of a typical planetary rover to explore Titan's surface chemistry and lower atmosphere, Refs. 2-4. Dragonfly is thus the second rotorcraft destined to explore a planetary body since the highly successful Mars Ingenuity Helicopter, Refs. 5-11. Figure 1 shows the relocatable Dragonfly lander scheduled to launch in 2028 with a planned Titan arrival in 2034. As an ocean world with abundant carbon rich chemistry, Titan promises planetary science data that may help us better understand the formation of life on Earth billions of years ago, Refs. 12-13.

As a multi-rotor vehicle, Dragonfly rotor aerodynamic performance is critical for overall science mission success. The rotor system is designed for the unique atmospheric and environmental conditions at Titan. Besides the high atmospheric density (440% of sea-level standard Earth air) and lower gravity (14% that on Earth), Titan's atmosphere is cryogenic (95 Kelvin, or -288 Fahrenheit). During descent to Titan, preparation to powered flight (PPF) de-spins the backshell using Dragonfly's rotors. The Dragonfly lander is then released from the backshell and transitions to powered flight (TPF) into a steady descent to Titan's surface. Powered by a multi-mission radioisotope thermoelectric generator (MMRTG) to recharge batteries, Dragonfly will perform a series of surface flights on Titan in subsequent years, Ref. 4.

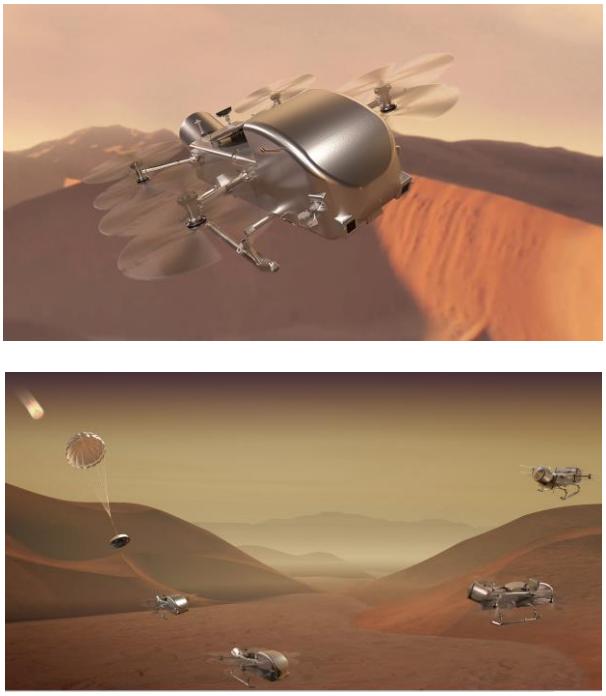

Figure 1. Dragonfly – Titan Relocatable Lander, NASA's 4th New Frontiers Mission. Image courtesy of NASA/Johns Hopkins APL/Steve Gribben (https://dragonfly.jhuapl.edu/Gallery/)

The rotor design is constrained by the aeroshell during transit to Titan. For the present work, a fixed-pitch speed-controlled two-bladed coaxial rotor system (Dragonfly Phase B*) was tested in the NASA Langley Transonic Dynamics Tunnel (TDT) in September 2022. The rotors have a diameter of 1.35 meters and an inter-rotor spacing of 25% of the rotor diameter (D/4). The rotor design balances power requirements in hover, climb, cruise, and descent for best overall mission performance of the fixed-pitch speed-controlled configuration. Since then, the rotor system has evolved to a three-bladed configuration with canted rotors and closer fore-aft rotor spacing along the sides of the lander, see Ref. 14. The

current three-bladed configuration (Phase C) has the same rotor solidity (at reduced chord) and mean inter-rotor spacing as the earlier two-bladed rotor system (Phase B*) reported in the present work. Indeed, this work supports, with insights gained from a Reynolds scaling analysis of conditions at Titan and those in the TDT, that rotor performance is expected to be nearly unaffected by these changes.

The paper is organized as follows: The section on 'Experimental Design' summarizes aspects of the test stand design and test matrix, scaling Titan conditions to the NASA TDT facility, and information on the data acquisition system and quantification of data uncertainty. Following that, the section on 'RotCFD - Hybrid BEMT/URANS Solver Methodology For Multirotors' is introduced, with a description of the model setup, C81 table generation, grid sensitivity studies, and the accuracy of computed performance metrics based on the scanned geometry of manufactured blades and including the sting arm between upper and lower rotors. A special section 'Scaling Phase B* Rotor Performance From TDT To Titan' presents a thorough analysis of rotor performance across the wide range in Reynolds number between the NASA TDT and anticipated flight conditions at Titan. The subsequent section on 'Quantitative Data Comparisons – RotCFD vs. TDT-HG' discusses in detail quantitative comparisons between the CFD tool and TDT test results for typical flight conditions during take-off, climb, cruise, descent, landing, as well as challenging conditions such as vortex-ring state (VRS). The last section is dedicated to 'Uncertainty Quantification For Mobility CLS' and presents an analysis of the predicted rotor performance uncertainty derived from the comparisons. The 'Conclusions' section summarizes the primary findings and contributions of this work including insights and recommendations for anticipated future tests for the NASA Dragonfly program.

- EXPERIMENTAL DESIGN – COAXIAL ROTOR TEST IN NASA TDT

NASA Langley Research Center Coaxial Rotor Test

The fixed-pitch speed-controlled coaxial rotor system (Dragonfly Phase B*) was tested in the NASA Langley TDT facility, Ref. 15. This TDT test was one in a series of wind tunnel tests supporting the NASA New Frontiers Mission Dragonfly, which uses a coaxial quadrotor configuration, see also Refs. 16-22 for other recent studies. The test stand as installed in the NASA TDT is shown in Fig. 2.

Though this test was specifically focused on Dragonfly's coaxial rotor system, the results from this test are relevant to a wide variety of multirotor vehicles, especially those using fixed-pitch variable-speed coaxial rotors, most notably are similar configurations for eVTOL aircraft and Unmanned Aerial Systems (UAS).

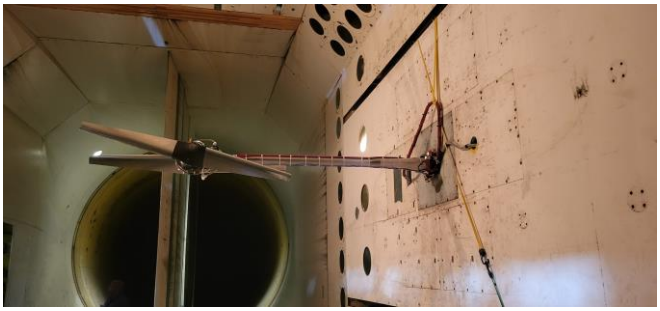

Figure 2. Nasa Langley Transonic Dynamics Tunnel (TDT) with Phase B* rotor installed in test section.

Scaling Titan Conditions to NASA TDT

The NASA Langley TDT is a closed-circuit, variable-pressure wind tunnel using either air or R-134a as a test fluid. Among a multitude of technologies that have been tested in the TDT, the facility has extensive experience in rotor performance and aeromechanics testing of helicopter and tiltrotors. It has a 16ft x 16ft test section and achieves Reynolds numbers of 3-10 x 10^6 /ft model. The NASA Langley TDT is particularly suited for full-scale 1:1 Dragonfly model rotor testing due to the high density of the R-134a test fluid (see Table 1 top, where 'Earth' refers to TDT-HG conditions).

In fact, the fluid density in TDT-HG conditions corresponds approximately to Titan density at 4km altitude. The high density in TDT-HG therefore results in dynamic loads on full-scale test hardware close to Titan conditions. The primary difference between (atmospheric) conditions at Titan and TDT-HG is the ambient temperature (Titan = Cryogenic at approx. 95K; Earth/TDT-HG = Ambient at approx. 305K). Consequently, the dynamic viscosity in TDT-HG is about 3x that at Titan, resulting in a Reynolds scale of approximately one-third compared to Titan conditions. For reference, tip section Reynolds number at Titan is about Re = 3x10^6 in hover/cruise, corresponding to Re = 1x10^6 in TDT-HG, thereby allowing good performance scaling from TDT-HG to Titan conditions. Also seen in Table 1 (top) are the speed of sound, a, both at Titan and TDT-HG conditions. TDT-HG has approximately 20% lower speed of sound compared to Titan, so Mach scaling is achieved at correspondingly lower tunnel speed (and RPM to match advance ratio) compared to Titan.

Given that tip Mach numbers of the full-scale model rotor do not exceed Ma = 0.4 (at max. RPM), the rotor aerodynamics is subject to only small compressibility effects. In summary, TDT-HG provides matched conditions for a full-scale (1:1) model rotor (Mach number, Ma; advance ratio, J; 1/3 Reynolds number, Re; 3/4 Lock number Lo) compared to Titan conditions. - As far as testing in air is concerned, i.e. TDT-Air (see Table 1 bottom), the resulting lower density and higher speed of sound in TDT-Air (compared to TDT-HG) necessitate testing at 2x tunnel speed and RPM in order to match Mach number and advance ratio, with an additional ½

Reynolds scale compared to TDT-HG (denoted as TDT in Table 1 bottom). In summary, TDT-Air provides matched conditions for a full-scale (1:1) model rotor (Mach number, Ma; advance ratio, J; 1/2 Reynolds number, Re; 1/3 Lock number Lo) compared to TDT-HG conditions.

Table 1. Scaling Titan conditions to TDT-HG (Top) and TDT-HG to TDT-Air (Bottom).

	Titan	Earth	TDT	
v (m/s)	10	8.34		
ω (rpm)	800	667		
r (m)	0.675	0.675		
T (K)	94	303.15	30 C, 86 F	
ρ (kg/m3)	5.3	4.04		
μ (Pa-s)	6.70E-06	1.24E-05		
P (atm)	1.44	1.0		
a (m/s)	203.3	169.5		
M	0.049	0.049	1	
Ma	0.278	0.278	1	
J	0.177	0.177	1	
Re	2.23E+06	7.68E+05	0.34	
Lo	3.70	2.82	0.76	

(or 14x22)

Dragonfly	TDT	TDT Air		
v (m/s)	9.4	18.8		
ω (rpm)	870	1740		
R (m)	0.675	0.675		
T (k)	303.15	303.15		
ρ (kg/m3)	4.04	1.225		
μ (Pa-s)	1.24E-05	1.81E-05		
P (atm)	1	1		
a (m/s)	169.5	343		
M	0.055	0.055	0.99	TDT Air/ TDT
Ma	0.363	0.359	0.99	
Advance Ratio	0.153	0.153	1.00	
Re	9.89E+05	4.11E+05	0.42	
Lo	7	2.1225248	0.30	
Thrust	NA	NA	1.21	
Power	NA	NA	2.43	

TDT Phase B* Coaxial Rotor Test Stand & Test Matrix

The Dragonfly Phase B* rotor has a diameter of 1.35 meters, a chord length of 0.156 meters at 10% root cutout, a taper ratio of 2.43, and a tri-linear twist distribution of 12.1 degrees. The rotor is equipped exclusively with the NACA 44-series airfoils chosen for robustness in Reynolds scaling, docile stall behavior, and low sensitivity to changes in surface roughness and probability of on-blade and tip vortex condensation of Titan atmospheric methane, see Ref. 23. The coaxial rotor system (Dragonfly Phase B*) was tested over a wide range of flight conditions from axial climb through edgewise flight and axial descent. Figure 3 shows a schematic of the TDT rotor test assembly (equipped with the Phase B* blade), including the KDE motors, load cells, and cooling plates. Also shown are a photograph of the test assembly as installed in the TDT along with a table of rotor configurations tested in HG (R-134a) and air. Full-scale model testing in HG (R-134a) allowed for testing at tunnel speeds similar to those that will be experienced by the rotors at Titan. This allowed the test matrix of the TDT test to be specified fairly close to the actual Dragonfly flight envelope. In general, the full range of shaft angles (i.e. -90deg in axial climb to +90deg in axial descent) is only encountered at low speed, while the range of shaft angles becomes constrained towards more shallow climb/descent and edgewise flight for increasing air speed where it is either limited by motor power/current draw (in climb, i.e. negative shaft angles) or the vortex ring state (VRS) and windmill brake state (WBS) boundaries (in descent, i.e. positive shaft angles).

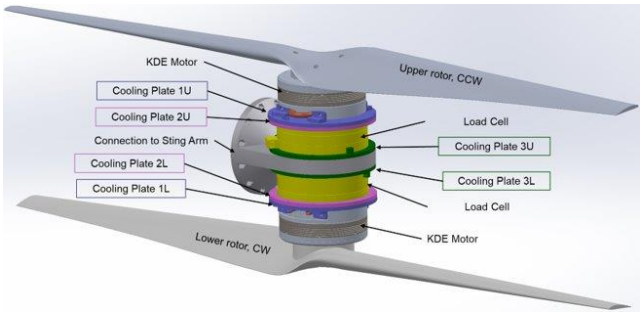

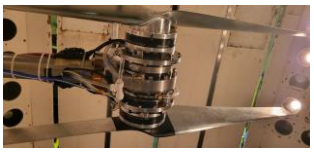

Configuration	HG	Air
coaxial	X	X
Single opposite fixed	X	
Upper Alone	X	X
Lower Alone	X	X
Rotor Off Tare	X	X

Figure 3. Phase B* Rotor Assembly & Test Matrix.

Data Acquisition System & Uncertainty Quantification

Two data acquisition computers (DAQ) were utilized in the test. The Pennsylvania State University (PSU) DAQ provided the model control and recorded the data from the ELMO ESC's, the load cells, thermocouples, encoders, optical sensors, and single axis accelerometers. The data acquisition rate was 2,000 samples per second. The TDT DAQ was cued from the PSU DAQ with a five-volt trigger signal to try and align the two data sets. The TDT DAQ was also running at 2,000 samples per second and recorded the tunnel parameters, and the single and tri-axis accelerometers.

Run numbers assigned by the TDT represented a desired velocity and shaft angle combination, or were used for tunnel static checks, zeroes, tunnel diagnostics, etc. Each individual velocity, shaft angle, and RPM data were acquired across both DAQs and automatically assigned a unique test point by the TDT that incremented throughout the duration of the test. The TDT data were provided as a function of the point number. Both time history and an averaged point summary file were provided from the TDT. The 2,000 Hz time history data were provided as .mat files and the point summaries were provided as Excel files. The PSU DAQ outputs provided time history files that had unique file names based on the motor one and two speeds, shaft angle, and tunnel velocity. These individual points were then filtered using a 0.25 second sliding average,

tare corrected, and consolidated into Excel files based on the configuration. Small sample sizes in the TDT data necessitated defining a custom uncertainty parameter δ in lieu of a traditional statistical confidence interval:

$$\delta = \sqrt{(\delta_{RA})^2 + (\delta_o)^2 + (\delta_i)^2 + (\delta_{LC})^2}$$

Here RA Ratio (δ_{RA}) is the ratio of the standard deviation of the ¼ second averaged signal to the mean. The RA Ratio thus effectively provides a 1σ confidence interval on the mean for a given data point. Repeatability (δ_i), or in-run repeatability, represents the spread of data points repeated within a given run (i.e. how much the loads vary for repeated RPMs at a given shaft angle + tunnel speed combination). It is calculated as the mean of the percent deviations from the mean of the in-run repeats. Reproducibility (δ_o), or out-of-run repeatability, represents the spread of measurements between repeat runs (i.e. how much the loads vary when a run is repeated at a later time). It is calculated as the mean of the percent deviations from the mean of the out-of-run repeats. The load cell uncertainty (δ_{LC}) is taken as the percentage of the resolution relative to the mean measurement. Note that the measurement uncertainty is already accounted for in the RA Ratio; the load cell uncertainty was added to account for limitations in the load cell resolution.

To capture the significant variations in δ across different flight regimes, the TDT test team reported a separate δ for each of six flight regimes (Steep/shallow climb, steep/shallow descent, VRS, and Hover). Indeed, the measured data uncertainty as shown in Figure 4 is nearly 2x in the steep versus respective shallow climb/descent conditions, particularly for the upper rotor. In this regard, the thrust uncertainty for the lower rotor appears a bit smaller compared to the upper rotor. In general, steep descent and VRS have the highest data uncertainties; these are attributed to unsteady aerodynamic interaction/loading effects that act in addition to the data uncertainties in typical steady-state flight conditions. Figure 4 further show that both scout and cruise are at the interface between edgewise flight and shallow climb.

Overall, it is important taking into account that data uncertainty itself is a function of different parts of the flight regime, as seen in Figure 4, which has some implications for subsequent quantitative comparisons against Computational Fluid Dynamics (CFD) rotor performance predictions.

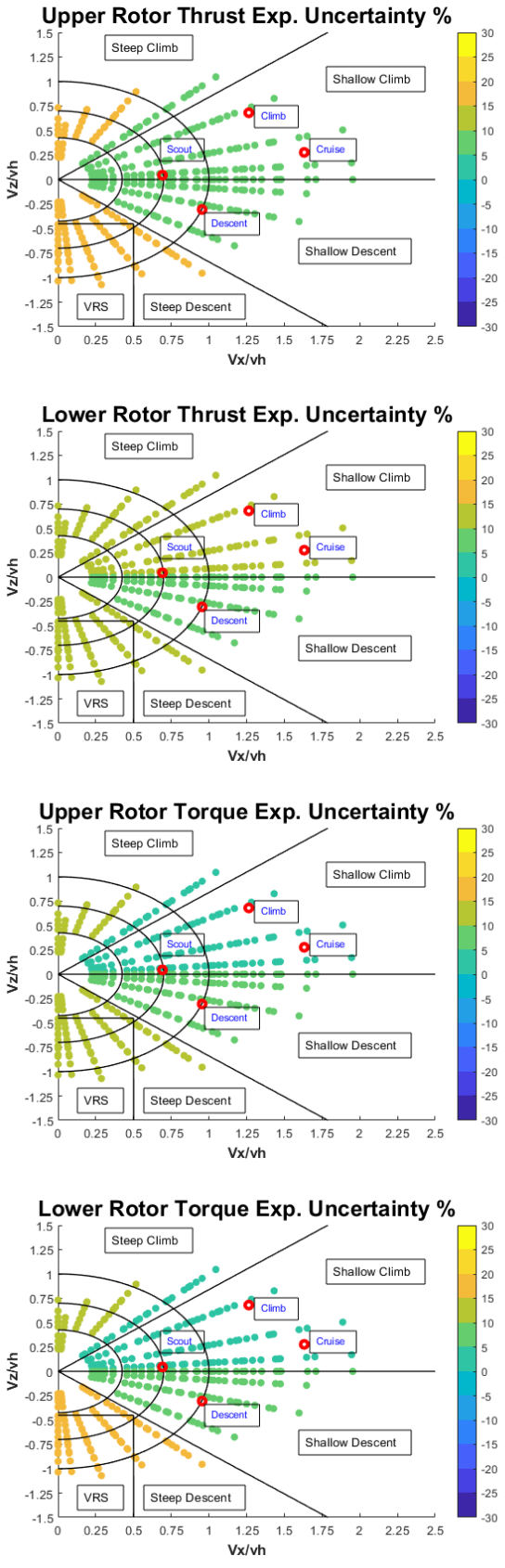

Figure 4. Experimental percent uncertainty for upper/lower rotor thrust/torque by rotor state.

ROTCFD - HYBRID BEMT-URANS CFD METHODOLOGY FOR MULTIROTORS

RotCFD – Rotorcraft Computational Fluid Dynamics

The RotCFD program, see Refs. 24-27, is based on a hybrid Blade Element Momentum Theory with Unsteady Reynolds-Averaged Navier-Stokes (BEMT-URANS) methodology, highlighted orange in the middle of Fig. 5.

The advantage of this methodology is that it combines the speed of a blade-modeled approach with the improved accuracy of a URANS CFD resolved inflow and wake. This provides a computational cost in between the low- and high-fidelity methods due to its blade-modeled description of the rotor. For time-averaged rotor performance metrics such as thrust, torque, roll moment, and pitching moment, this method provides very good accuracy in rotor performance predictions. Although more expensive blade-resolved models can provide more accurate information in the form of a time-accurate solution (though not always, see Ref. 28), a very carefully constructed model of the rotor blade and its cross-sectional (two-dimensional) airfoil performance provides accurate results for the time-averaged values relevant to the flight control system.

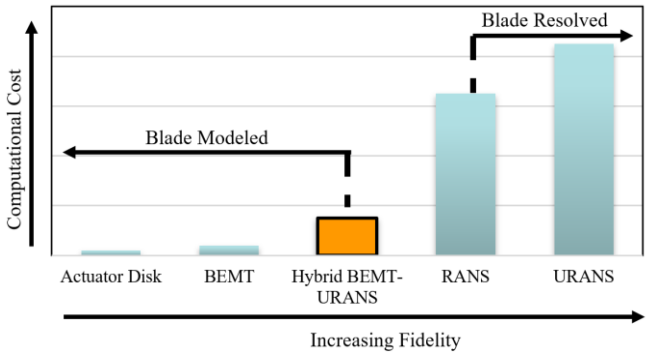

Figure 5. Computational Cost vs. Model Fidelity for Various Rotor Analysis Approaches.

In particular, the program uses a BEMT rotor model interfaced with a finite-volume structured cartesian grid system that uses implicit time integration to solve the incompressible URANS equations with a two-equation k-ϵ turbulence closure and the SIMPLE-based solution method, see Ref. 29. As compared to a lower-order blade-modeled approach with an inflow model, the URANS flowfield resolves the actual rotor inflow and wake trajectory in various flight conditions, as well as capturing of rotor-rotor and rotor-airframe interactions. The BEMT rotor model and URANS grid system are interfaced together using an actuator disk with distributed momentum sources. The URANS grid is used to calculate inflow over the entire rotor disk, which is then passed to the BEMT rotor model for use with C81 airfoil performance lookup tables. The BEMT model results are time-averaged to further reduce computational cost but retain good azimuthal accuracy to capture e.g. retreating blade stall and advancing blade compressibility effects.

The resulting BEMT sectional forces are then applied back into the URANS flowfield through distributed momentum sources in the actuator disk. This allows for the rotor performance to be accurately modeled with a several order of magnitude reduction in computational cost compared to blade-resolved CFD. To include additional geometry, such as rotor hubs or an airframe, tetrahedral body-fitted cells can be implemented and have been used in the present work to model the wind tunnel test assembly, see Fig. 6. The refinement of these cells is not typically sufficient to develop the boundary layer on any included geometry, so wall functions are used. The RotCFD model was constructed to mimic the experimental test article as closely as possible; wind tunnel walls were not modeled as their effect was estimated to be small compared to all other data uncertainties. Since the URANS flow solver on the structured grid is not resolving any boundary layers, a coarse description of the geometry can be used. As shown in Fig. 6, the basic shapes of the model sting, motors, load cells, and mounting hardware are approximated to adequately capture blockage effects.

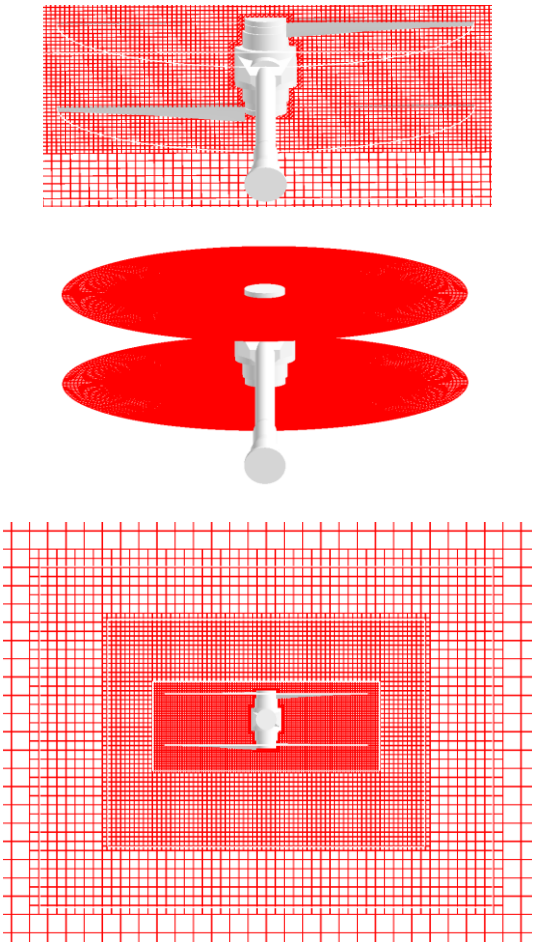

Figure 6. RotCFD Phase B* Rotor Grid.

RotCFD Model Setup & C81 Airfoil Table Generation

The rotor twist and chord distributions were discretized (uniformly) every 2.5% of the blade radius from the root cut-out to the blade tip. The grid resolution is maintained slightly downstream of the rotors, but since the solver is not modeling blade tip vortices, the grid can be coarsened at a moderate pace moving away from the rotors. To properly account for the effects of blade-tip losses, a linear tip-loss model was used. The model linearly drops the thrust produced from the value at a user-specified location to zero at the tip. The

starting point for this linear tip loss was selected in order to give the same total thrust degradation as would a Prandtl tip loss. Figure 6 shows more of the flow domain of the TDT RotCFD grid, which has its far-field boundary at 10 rotor diameters in every direction away from the model. The boundaries have 14 cells along their 27-meter length, resulting in the largest cell size being about 1.93m cubed. The grid refinement around the coaxial system is held constant with eight steps down from the boundary, halving the cell size in all three dimensions at each step. This results in a cell size near the model of approximately 15 cm cubed. This cell refinement yields about 90 cells across the diameter of the rotors, which has been developed as a best practice gridding approach in several past studies, see Refs. 16, 26, 28.

Standard best practices were followed for the C81 table generation in OVERFLOW (Ref. 30). Here a grid refinement study was also carried out following the procedure specified in Ref. 28. As such, the rotor blade was discretized into 13 radial stations from blade root to tip. The final O-grid topology around a section airfoil and blunt trailing edge is shown in Fig. 7. All C81 tables have thus far been run fully-turbulent (Spalart-Allmaras turbulence model, Ref. 31).

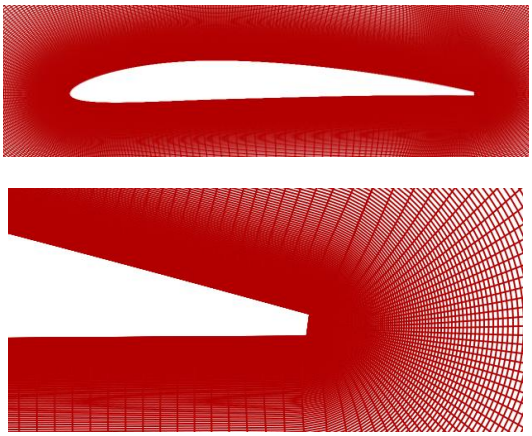

Figure 7. O-Grid around NACA 4412 airfoil with close-up of trailing edge.

The C81 Generator simulations were run over an angle-of-attack range between -20 and +20 degrees. Outside this range (following standard practice), the C81 airfoil tables use NACA 0012 experimental data at the appropriate Reynolds number as an approximation of airfoil performance beyond stall, where the airfoil performs practically as a flat plate. This sweep was simulated at various Mach and Reynolds number combinations, which captures the changing airfoil section performance with changing rotor speed. The full C81 airfoil performance deck for this rotor uses approximately 3,000 OVERFLOW simulations, which were scripted to be massively parallelized on the NASA High-End Compute Capability (i.e. the NASA supercomputers). Airfoil input decks were generated for both the R134-a heavy gas and air test environments, which represents approximately 6,000 distinct OVERFLOW airfoil calculations.

Grid Sensitivity Study

A formal grid resolution study was conducted to verify that best practices were adequate. For the grid resolution study, the number of cells at the boundary were adjusted to increase or decrease the total number of cells in the simulation as well as the resolution of the cells surrounding the rotor system. Figure 8 shows representative results of this study for both upper/lower and coaxial rotor power in hover and cruise.

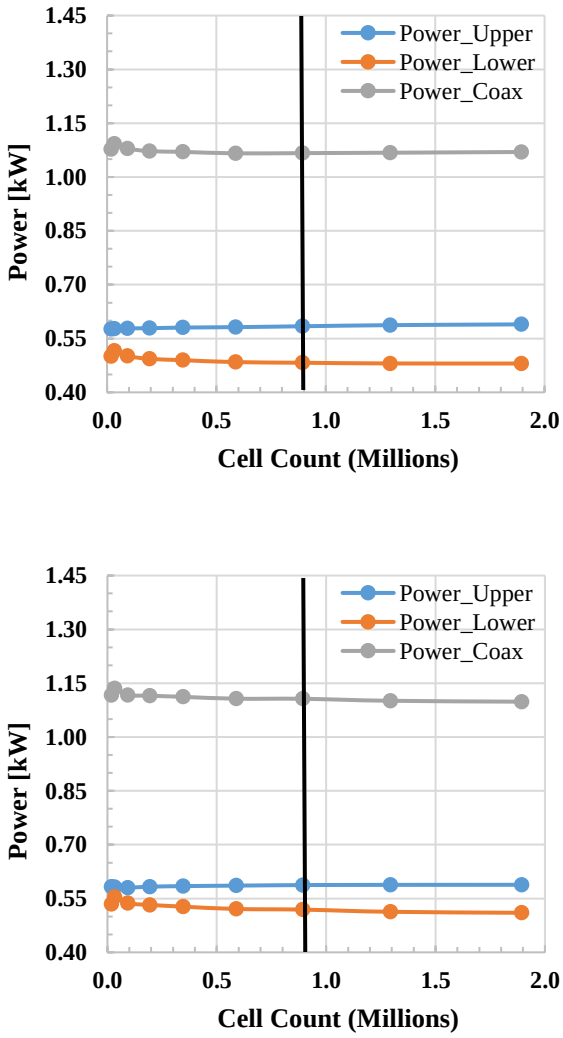

Figure 8. Example Grid Resolution Study – Power. (Top: Hover, Bottom: Cruise)

The baseline grid has approximately 890 thousand cells. The coarsest grid has 18 thousand, and the most refined grid has 1.9 million cells; note here that the 18 thousand cells grid has a very coarse Cartesian grid away from the rotor but still comparable resolution around the rotor. The change in coaxial power between the baseline and most refined grid is within 0.3% for hover 0.7% in a typical Dragonfly cruise condition. The baseline grid resolution was chosen to balance solution accuracy with computational cost. These changes are indeed smaller than quantitative differences between rotor

performance predictions (RotCFD) and measured TDT-HG data, as is discussed in a later section.

Rotor Geometry Verification

The CFD rotor model as described in the previous section was generated based on exact rotor design specifications for blade chord, twist, and C81 tables, with RotCFD runs conducted prior to the wind tunnel entry. After the TDT experiment, both tested blades (Blade 1 = upper rotor; Blade 2 = lower rotor) and a respective spare blade (not tested) were scanned in order to quantify possible twist alterations and out-of-plane blade deviations as a result of the blade manufacturing process. These 3D blade scans were conducted in-house at the Johns Hopkins University Applied Physics Lab (JHUAPL). The 3D scans were conducted using a Nikon K-scan MMDx with handheld laser scanner and single point accuracy ~ 0.04" (0.10 mm). Sublimating developer spray was used to reduce surface reflectivity to improve measurement precision. Pressure and suction sides of the rotors were scanned separately with >50% overlapping scan areas to facilitate scan alignment. The two scan portions were then merged using a K-scan software linear regression best fit. Merged scans were aligned to the nominal model using the Geomagic Control built in "best fit alignment" feature. A total of 13 stations were defined as planar cross sections located radially along the blade axis. Rotational and translational offsets were measured at each cross section using the Geomagic Control's built-in twist analysis. The twist analysis function used a first-order approximation of Euclidean distance for best fit analysis. It then reported the in-plane translation and rotation of the scan data needed to perform that fit.

It was found that the out-of-plane blade bending as a result of the manufacturing had resulted in tip deflection approx. equal to the blade tip thickness (i.e. order 5mm). This essentially adds a small coning (or dihedral) to the blade planform. In order to bound the problem from a computational standpoint, a small coning angle of 0.6 deg was added to the RotCFD model in addition to taking the maximum twist warp (approx. 0.2 deg) associated with the scanned blade. Following, the resultant altered RotCFD model was run for representative flight conditions including hover, cruise, scout, climb, and descent. Quantitative analyses showed that performance deltas for rotor thrust and power were all within 1.5% compared to the baseline RotCFD model. It was decided that these quantified discrepancies would be tracked in the program as an additional CFD uncertainty.

Effect of Sting Arm on Rotor Performance

A further CFD model uncertainty study was conducted to quantify the effect of the rotor sting on rotor performance compared to the baseline configuration of an isolated rotor pair (i.e. hub and shaft only) as used for the full CFD performance matrix. In Figure 9, these configurations are shown (blue, orange) alongside a third configuration of a front-aft coaxial rotor pair (grey). In the following, we focus on Configurations 1 and 2 as depicted in Figure 9 as those are the ones relevant for the TDT data comparisons (Configuration 3 in Figure 9 was part of a different study).

A limited study was performed for a cruise, scout, and steep descent condition (with the scout condition not shown in this paper as it exhibited results consistent with the cruise condition). Steep descent was considered at 4.7m/s and cruise at 9.5m/s air speed. Figure 9 also shows the respective shaft angles and rotor speeds for the specific conditions provided by the Mobility team and a breakdown into upper/lower and combined coaxial rotor thrust/power. As cruise and steep descent are disparate flight conditions with respect to the rotor inflow, one can expect that the effect of the sting arm between the rotors results in different trends of the effects on rotor thrust and power due to a difference in rotor/sting-arm interactional aerodynamics effects.

Indeed, including the sting arm for the steep descent condition results in a total of +2.85% additional coaxial rotor thrust, while reducing rotor power by as much as 8.8%. Note here that power requirements in descent are only about ¼ of power required in cruise; hence the seemingly high percentage has to be seen in conjunction with absolute numbers in Watts. For cruise, combined rotor thrust reduces by 1.7% when including the sting arm, while combined rotor power increases by 2.5%.

Therefore, no clear trend becomes apparent when including the sting arm, a mere effect of differences in interactional aerodynamics for the disparate flight conditions chosen for this limited study. Anticipating here similar flight conditions that are documented in a later section on quantitative comparisons, it was found that including the sting arm has improved the comparisons against TDT experimental data. It was therefore recommended that the sting arm located between the upper/lower rotors be included in the full RotCFD performance matrix for subsequent quantitative comparisons against measured TDT data as its interactional aerodynamics effects are appreciable from the perspective of rotor performance prediction.

SCALING PHASE B* ROTOR PERFORMANCE FROM TDT TO TITAN

The NASA Langley TDT provides scaled conditions for a 1:1 Dragonfly Phase B* rotor system in terms of Mach number, advance ratio, and Lock number at a fluid density of approx. 75% that at Titan (when testing in heavy-gas R-134a, i.e. TDT-HG), with the Reynolds number being the sole parameter that can only be matched to one-third in the TDT when compared to Titan conditions, a consequence of fluid kinematic viscosity at 300K in the TDT versus 90K at Titan). In the absence of any possibility of a flight test at true Titan conditions prior to launch, the question arises about how to ensure that a Titan rotor performance matrix as computed by RotCFD (or any other computational analysis tool) predicts the actual rotor performance at Titan within desired confidence levels. Indeed, the robustness to Reynolds scaling

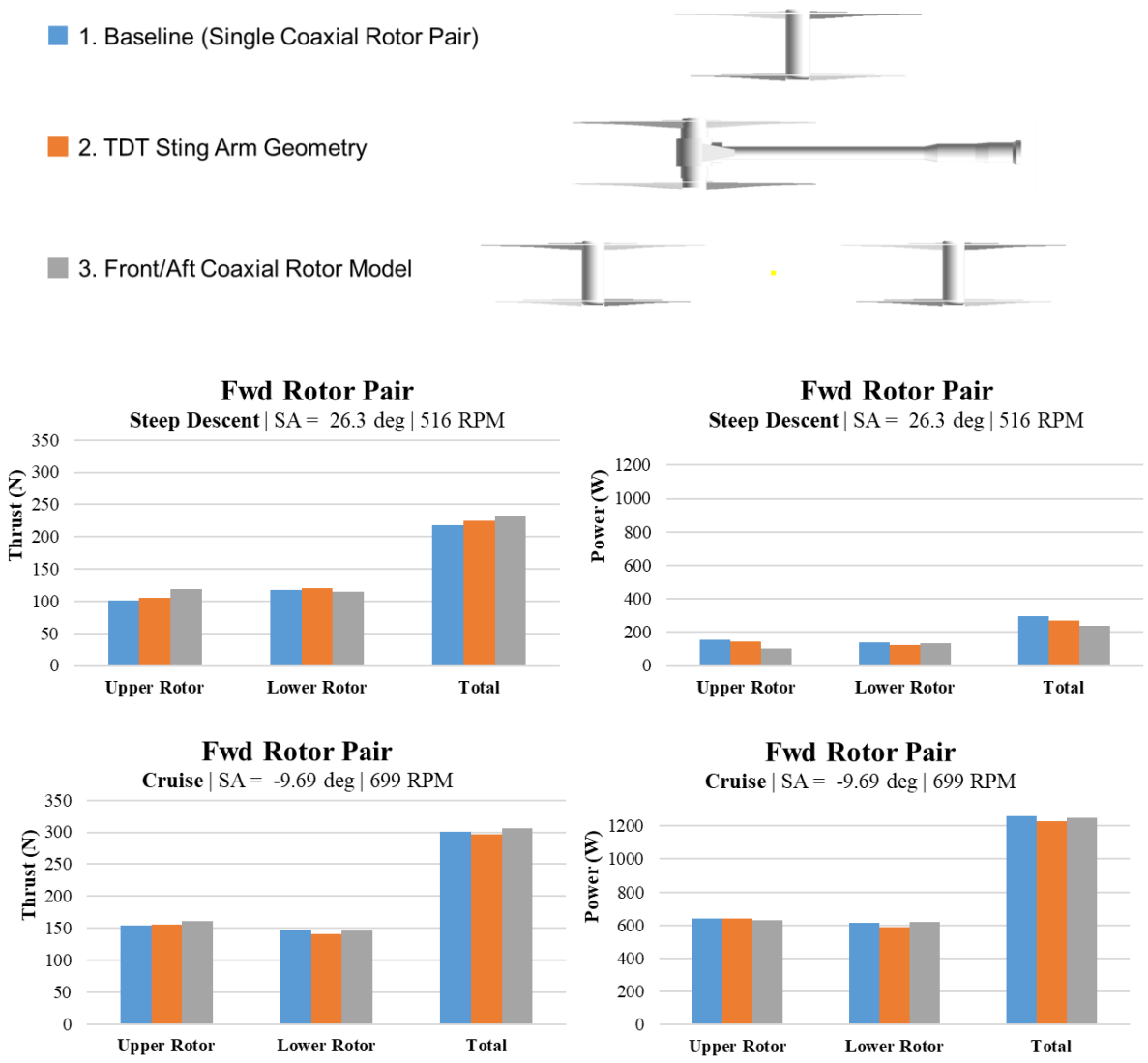

Figure 9. Effect of CFD Configuration on Rotor Performance.
(Blue = Baseline Coax, Orange = TDT Sting Arm, Grey = Front/Aft Coax)

between TDT-HG and Titan was one of the reasons for choosing the particular airfoil series for the Phase B* rotor.

Consequently, as documented in later sections, the main uncertainty applied to the computed Titan rotor performance matrix (and used by the Mobility team) is driven by comparisons between computed and experimental data in the TDT, while it is shown that scaling from TDT-HG to Titan conditions has notably smaller uncertainty.

Scaling Phase B* Rotor from TDT-HG to Titan

As mentioned above, the Phase B* rotor was designed with the objective of being able to reliably scale its performance from TDT-HG to Titan conditions. This constraint contributed to choosing the NACA 44## airfoil series to be used for the Dragonfly Phase B* rotor. In general, the reasons for using this airfoil series are: i) robustness to scaling from TDT-HG to Titan, ii) docile stall behavior, iii) low sensitivity to changes in surface roughness, iv) large trailing-edge angle for blade manufacturing, v) available experimental data for roughness and high angles of attack, and vi) large range in available airfoil thicknesses for blade stiffness requirements.

Figure 10 shows example excerpts of the C81 OVERFLOW tables at TDT-HG and Titan conditions. Here station 10 (NACA 4415) is chosen as a representative high-thrust station on the advancing side. For reference, the medium Mach number in the plots corresponds to a trimmed cruise-type condition of 9m/s for the rotor system; the small difference between the Mach numbers in TDT-HG (Ma=0.29) versus Titan (Ma=0.24) is due to the difference in speed of sound (see also Table 1) for the given cruise speed. In general, it can be seen in Figure 10 that small compressibility effects associated with the Mach range of the Phase B* rotor system

are present, but that corresponding lift curves in TDT-HG versus Titan do have very similar behavior despite the disparate one-third Reynolds number in TDT-HG.

A direct comparison between TDT-HG and Titan conditions for Station 10 (C81 OVERFLOW table) is shown in Figure 11. It can be seen that the lift curves indeed overlap exactly over a wide range of operating lift coefficients (i.e. -0.7 – +1.4) which suggests that the induced power of the Phase B* rotor system is expected to scale well between TDT-HG and Titan conditions. Some additional observations in Figure 11 that are relevant for the scaling process are: i) Maximum lift coefficient is approx. 0.15 higher at Titan compared to TDT-HG (as expected by the difference in Re scale), ii) Drag coefficient at Titan is approx. 15% lower at Titan compared to TDT-HG (also as expected by the difference in Re scale).

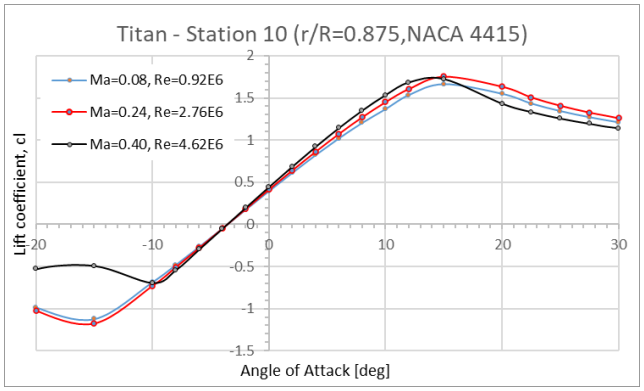

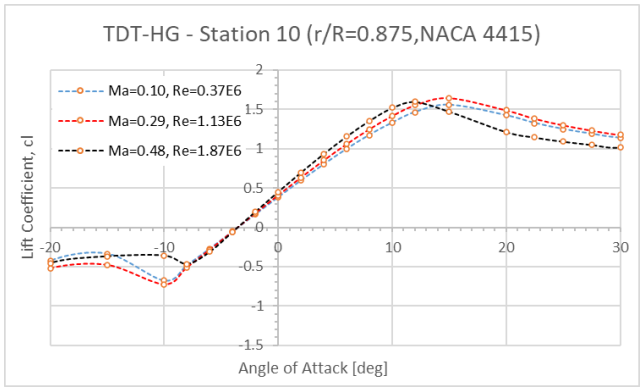

Figure 10. C81 Tables – Titan vs TDT-HG (Phase B* rotor, Station 10, Compressibility Effects).

The observations from Station 10 airfoil tables give rise to the following expectation for rotor performance: i) Thrust coefficient C_T is expected to scale well between TDT-HG and Titan for steep/shallow climb (i.e. SA = -90deg to -15deg), with a small discrepancy growing into descent and particularly steep descent (SA > +30deg) at high C_T and some sections experiencing beginning stall; ii) Torque coefficient C_Q may be expected slightly lower at Titan compared to TDT-HG due to lower profile drag associated with higher Reynolds number (3x) at Titan.

In the following, quantitative comparisons between RotCFD predicted rotor performance in TDT-HG versus at Titan are conducted in terms of dimensionless performance coefficients (i.e. thrust coefficient C_T, torque coefficient C_Q, and edgewise advance ratio μ_x). Using dimensionless performance coefficients is best suited for scaling purposes as those are normalized by fluid density, thus accounting for the respective differences between TDT-HG and Titan in the comparisons. The resulting dimensionless coefficients can then be used to assess Reynolds scaling effects on rotor performance in conjunction with associated C81 OVERFLOW tables.

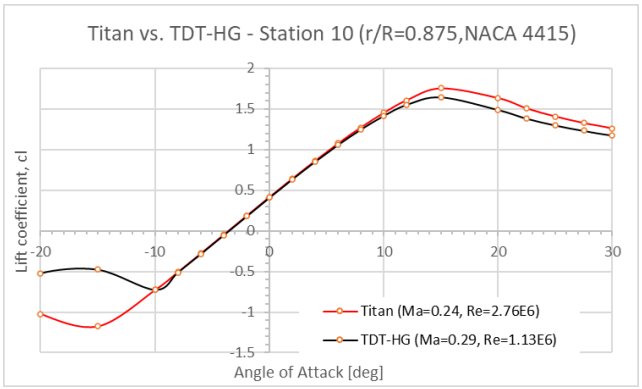

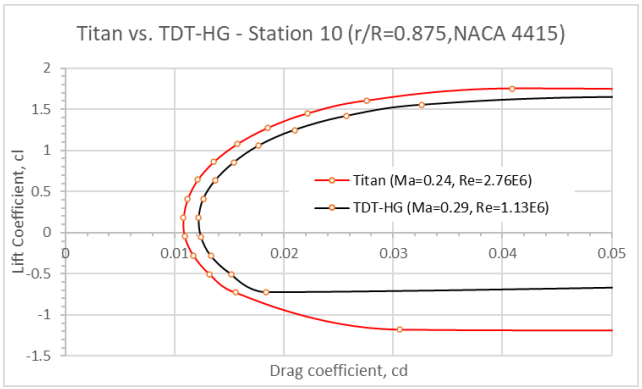

Figure 11. C81 Tables – Titan vs TDT-HG (Phase B* rotor, Station 10, Ma scaled).

Coaxial rotor performance comparisons in terms of C_T, C_Q, and μ_x are presented in the following way:

Shaft Angles (SA): -90,-85,-75,-60,-45,-30,-15,-5,0,+5,+15, +30,+45,+60,+75,+85,+90deg

- C_Q vs. C_T : Allows to see for which SA and rotor speeds the performance parameters collapse onto one curve. Also illustrates the beginning of WBS for $C_Q < 0$.
- C_T vs. μ_x : Illustrates C_T dependence on SA relevant to wake skew. Also shows relationship between SA and μ_x
- C_Q vs. μ_x : Illustrates C_Q dependence on SA. Also illustrates the beginning of WBS for $C_Q < 0$.

Figure 12 shows Ma-scaled RotCFD rotor performance results in TDT-HG and at Titan for a cruise speed and all shaft angles. Though all shaft angles are shown here, only approx. -30deg < SA < +30deg are relevant for flight at cruise speed due to torque/power constraints. Focusing first on the C_T vs. μ_x plot (middle in Fig. 12), it becomes apparent that the inner curves correspond to the higher rotor speeds (and hence lower μ_x). Furthermore, C_T increases with increasing SA from axial climb (-90deg) to edgewise flight (0deg) and up to axial descent (+90deg); this behavior is consistent with what would be expected of a fixed-pitch rotor applied to a wide SA range at constant RPM and airspeed. As for the C_Q vs. C_T, μ_x plots in Fig. 12, note that all results $C_Q < 0$ are WBS cases, which are practically not relevant for the flight envelope (though are shown here for completeness). It is noteworthy to mention that the C_Q vs. C_T curve nearly collapses for all cases, while the C_Q vs. μ_x curves are separated from each other for the respective pairs of rotor speeds. Rotor C_Q is highest in climb (at around SA = -15deg) as would be expected; also, C_Q at SA = -90deg (axial climb) is notably higher than C_Q at SA = +90deg (axial descent) as expected by basic power relations at constant rotor speed.

Comparing computed RotCFD rotor C_T and C_Q in TDT-HG and at Titan conditions in Fig. 12, it is apparent that C_T and C_Q practically collapse (< 5% discrepancy) between both Re environments for -90deg < SA < +30deg. The largest discrepancies are found for SA > +45deg, as expected, and are attributed to high-C_T effects and associated high lift coefficients c_l with some beginning inboard blade section stall, thereby revealing the difference in $c_{l,max}$, see Fig. 11. This is an important result as it gives confidence in the Phase B* rotor design methodology as well as airfoil choice to allow Re scaling to the Titan environment which cannot be reproduced for a 1:1 model rotor test on Earth.

The Mach scaled conditions between TDT-HG and Titan in Fig. 12 can be relaxed to match airspeed in both environments (as typically used by the Mobility team). The associated RotCFD results in TDT-HG and at Titan for the same pairs of airspeed and rotor speed (RPM) are shown in Fig. 13. Note that these comparisons now show the TDT-HG results at an approx. 20% higher Mach number compared to those at Titan, see the C81 tables in Fig. 10 as a reference at about 900 RPM. Comparing Fig. 12 (Ma scaled) to Fig. 13 (same airspeed), it is interesting to see that there is practically very little (if any) change in the C_T, C_Q curves when contrasting TDT-HG and Titan conditions for the RotCFD results. This gives rise to the conclusion that scaling from TDT-HG to Titan can be performed at the same airspeed and RPM, and the resulting small discrepancy in Mach scaling has little effect on the non-dimensional performance coefficients.

The preceding comparisons confirm that there is good understanding of the difference of Phase B* rotor performance in TDT-HG versus at Titan. As mentioned earlier in this section, it appears that the overall uncertainty in Phase B* rotor performance is driven by comparisons between computed and experimental data in the TDT and not by scaling from TDT-HG to Titan conditions. This strongly supports the notion that the Dragonfly Mobility team can rely on RotCFD predictions performed at Titan conditions, with uncertainties derived from TDT-HG comparisons between RotCFD and measured data as shown in later sections.

Scaling Phase B* Rotor from TDT-Air to TDT-HG

The challenge of not being able to test Phase B* rotors (or any Dragonfly prototype rotors) at full-scale Reynolds number as experienced in the Titan environment (see also earlier section), prompted the design of a sub-experiment in the TDT that simulated the process of scaling between two flow environments of disparate Reynolds number. Here a submatrix of test points was conducted in the TDT with air as the test fluid (i.e. TDT-Air). This not only allowed the test team to conduct shakedown tests of the assembly with easy access to the test section and no need for emptying/filling the tunnel with R-134a, but it also provided an opportunity for simulating the 'TDT-HG to Titan' scaling by conducting a limited experiment of 'TDT-Air to TDT-HG' scaling.

Following the scaling properties in Table 1 between Air and HG, a Ma-scaled experiment 'TDT-Air to TDT-HG' becomes feasible when the TDT-Air test is conducted at approximately 2x tunnel speed (and 2x RPM, to match advance ratio) compared to the TDT-HG. In such a case (see again Table 1), the TDT-HG cases are at 2x Reynolds number compared to the TDT-Air cases, yet matched Mach number and advance ratio. Consequently, the argument is that a 2x Re-scale step between TDT-Air to TDT-HG to a good extent represents a 3x Re-scale step between TDT-HG to Titan. The advantage of the 'TDT-Air to TDT-HG' test, in contrast to the 'TDT-HG to Titan' step, is that actual measured data are available in both environments. This of course assumes that the rotor aerodynamic characteristics in terms of C_T and C_Q are minimally affected by the additional lower Re-scale, now $1/6^{th}$x in TDT-Air compared to Titan.

Figure 14 shows experimental data acquired in TDT-Air versus TDT-HG for a Re-scaling study at an equivalent scout condition. The dimensionless performance coefficients C_T and C_Q are presented in the same way as in the previous section. It is reassuring to see that C_T and C_Q practically collapse between TDT-Air and TDT-HG, despite the 2x additional Reynolds scale. This gives initial confidence that Phase B* rotor performance is indeed consistent over a wide range of Reynolds numbers (as accounted for in the rotor aerodynamic design) and that a three-bladed Phase C rotor system at two-third blade chord is expected to also exhibit consistent performance in TDT-HG and at Titan. It further implies that discrepancies quantified between CFD (here RotCFD) and experiments in TDT-HG also translate to CFD rotor performance tables at Titan, as used in Mobility CLS.

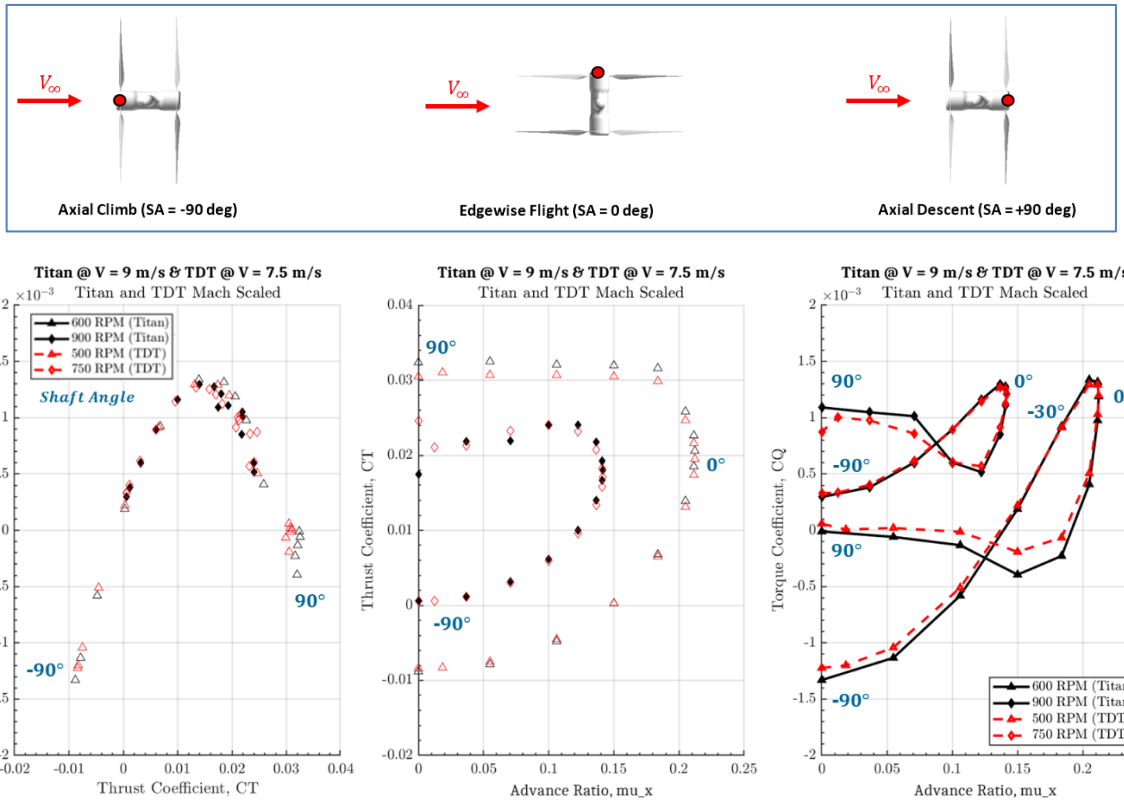

Figure 12. RotCFD – Titan vs TDT-HG (Full SA range, CRUISE speed, Mach scaled).

Shaft Angles: -90,-85,-75,-60,-45,-30,-15,-5,0,+5,+15,+30,+45,+60,+75,+85,+90deg

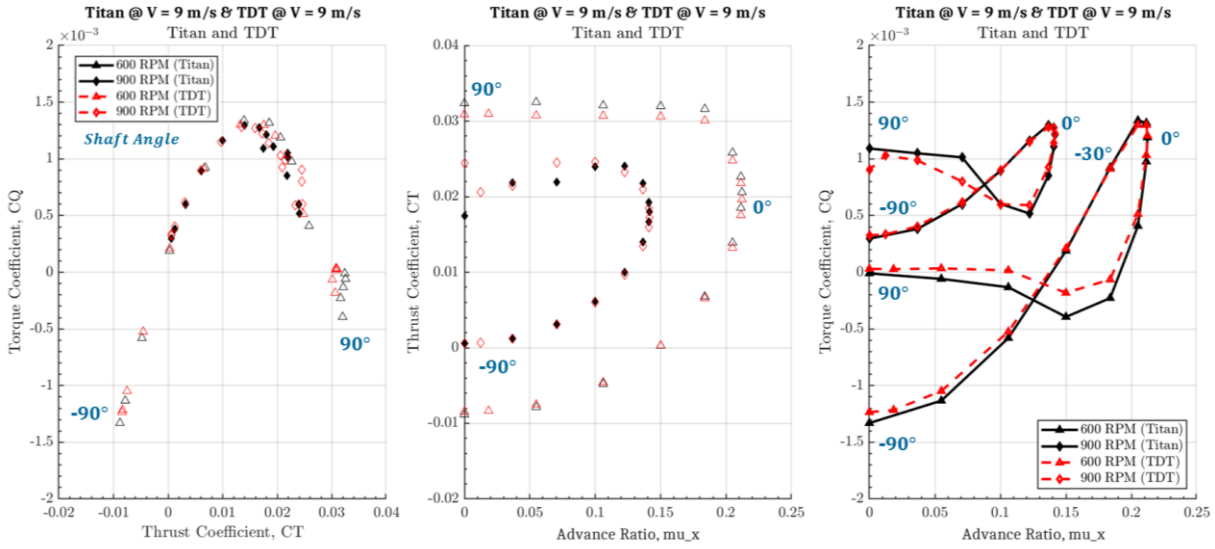

Figure 13. RotCFD – Titan vs TDT-HG (Full SA range, CRUISE speed).

Shaft Angles: -90,-85,-75,-60,-45,-30,-15,-5,0,+5,+15,+30,+45,+60,+75,+85,+90deg

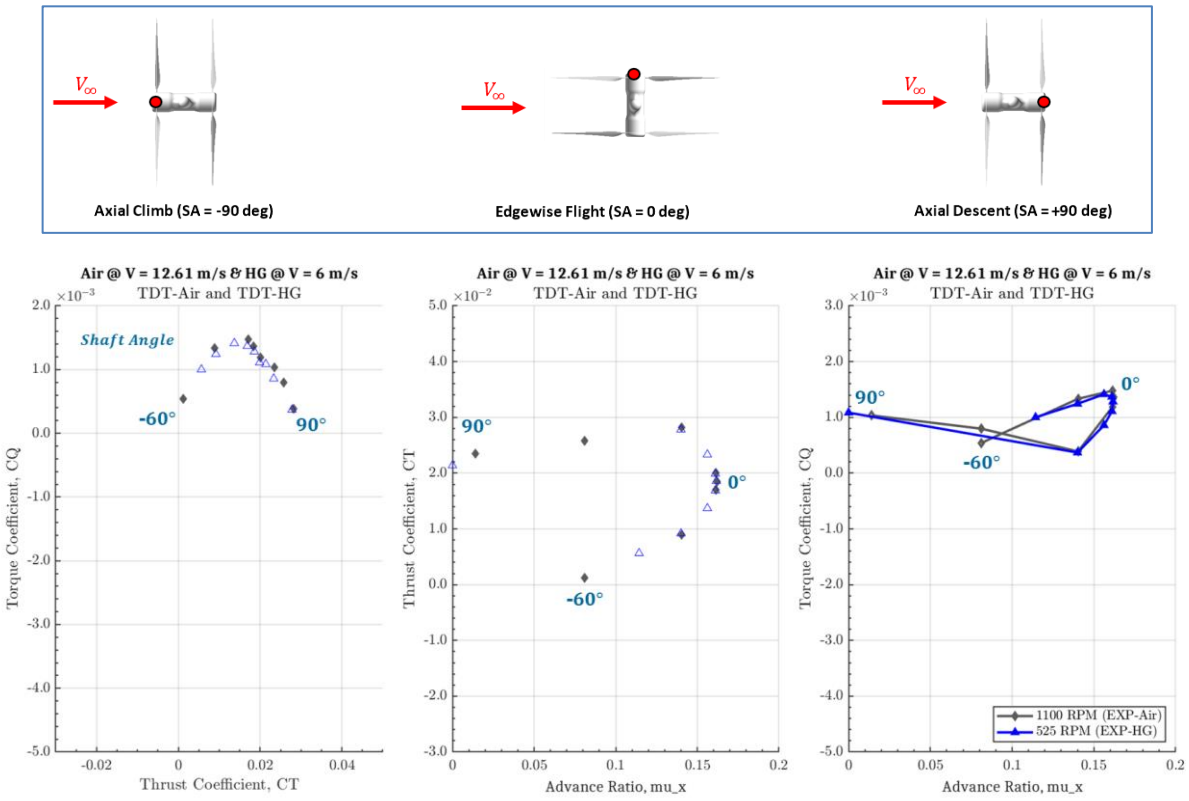

Figure 14. Exp. Data – TDT-Air vs TDT-HG (SCOUT speed, Mach scaled, 2x Re in TDT-HG).

Shaft Angles: -60,-45,-30,-15-5,0,+5,+15,+30,+60,+90deg

- QUANTITATIVE DATA COMPARISONS - ROTCFD VS. TDT-HG

This section focuses on quantitative comparisons between computed RotCFD rotor performance and measured TDT data in R-134a 'heavy gas' (i.e. TDT-HG). The comparisons are presented and discussed to encompass the disparate range of flight conditions for the fixed-pitch variable-speed Phase B* rotor. A representation of the various rotor states and flight envelope is shown in Fig. 15 for context. Here the purpose is to illustrate the primary rotor operating conditions as used in Mobility CLS, i.e. 'blue shaded' region in Fig. 15 (top) and the steady-state flight envelope in Fig. 15 (bottom). It can be seen that many data points have been measured and taken outside the typical regime, which has to be taken into account when quantifying the discrepancies between predicted RotCFD rotor performance and measured TDT-HG data.

Hover Conditions – Phase B* Rotor in TDT-HG

Comparisons of RotCFD rotor performance predictions in hover to the experimentally obtained TDT-HG data are reported in Fig. 16. Experimental wind tunnel data for wind-off conditions were obtained through a full sweep of shaft angles in the test section. To mitigate the chance of experimental measurement uncertainty skewing the results (as the TDT is not an ideal hover chamber), the experimental wind-off values for multiple shaft angles were averaged to obtain the experimental hover data used in the plots. Shaft angles corresponding to -90, -85, -75, -60, 60, 75, 85, and 90 degrees were used. Measured thrust and torque values for these various shaft angles showed discrepancies of order 5%.

Though the -90 and 90 degrees cases are most resembling idealized hover conditions, the averaged approach was taken to quantify the overall variation when compared to RotCFD simulations that did not include any tunnel walls (as described in an earlier section). The top and middle plots in Fig. 16 show rotor thrust versus RPM and rotor torque versus RPM, respectively. The upper and lower rotor thrust delta comparison errors were quantified as 2.6% and 3.4%, respectively. This means RotCFD slightly over-predicts individual rotor thrust compared to TDT-HG data. The largest single value is the lower rotor at 1100 RPM, at 9.5%. The torque comparisons are -4.4% and 0.5% for the upper and lower rotors, respectively, meaning the upper rotor torque is slightly under-predicted. The combined upper/lower coaxial rotor thrust in hover is predicted within an average of 2.9%, while the combined upper/lower coaxial rotor power (rotor

torques add with opposite signs) is predicted within an average of -2.3% compared to measured TDT-HG data.

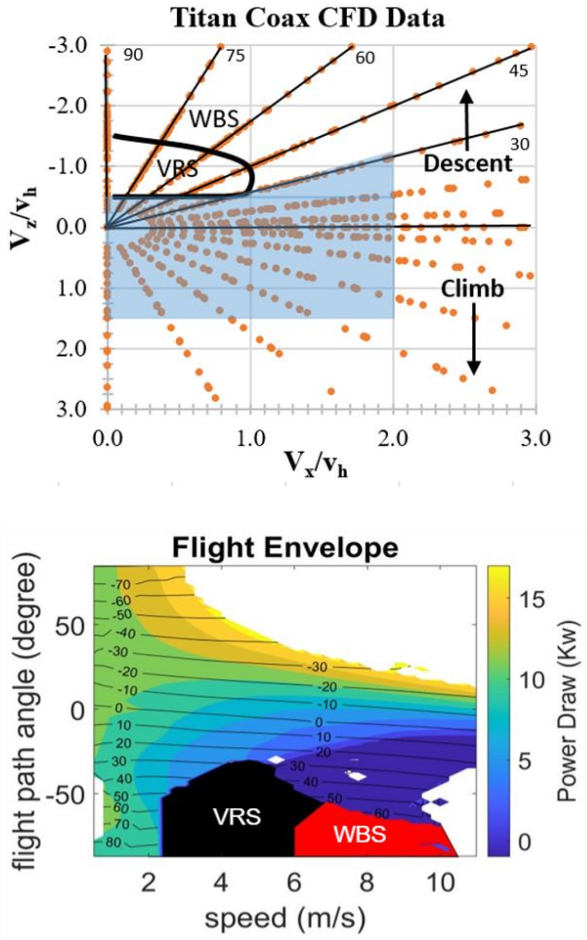

Figure 15. Dragonfly Phase B* rotor operating states and steady-state flight envelope.

Figure 16 (bottom) compares the RotCFD predicted coaxial figure of merit (FM) to the experimentally measured value. Here FM was calculated using combined values of thrust and power for each of the CFD and experimental conditions. The figure of merit comparisons are within 6.8% (or approx. 5 counts in FM), with RotCFD over-predicting the coaxial rotor system's hovering efficiency as a result of over-predicting thrust by order 3% and under-predicting power order 2.5-3.0%. In general, the FM over-prediction increases for the higher rotor speeds, while FM predictions are within 2 counts of FM at 600 and 750 RPM (i.e. close to the design point). Note that FM is a sensitive performance figure, and data uncertainties based on thrust measurements in Figure 4 amount to an FM uncertainty of order 3-6 counts on their own. Furthermore, the NASA TDT is not an ideal hover facility, and RotCFD with its actuator-disk implementation is not a high-fidelity hover prediction tool. Nevertheless, quantitative comparisons are considered quite good for this purpose.

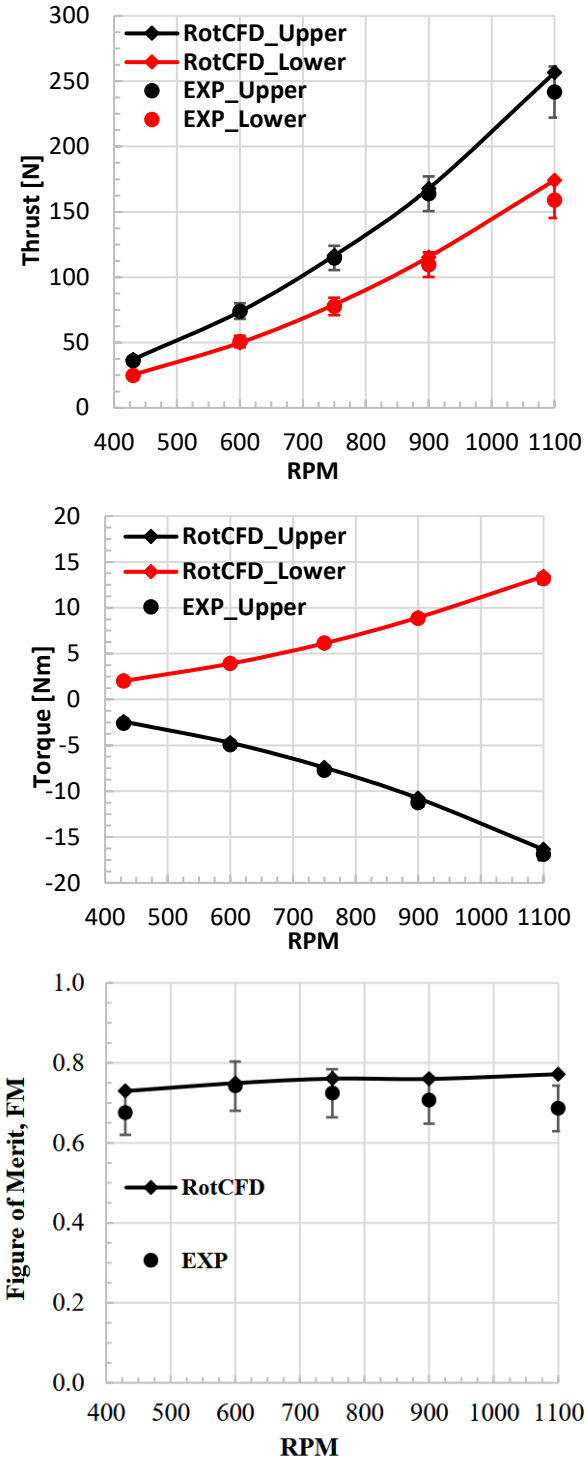

Figure 16. RotCFD vs. TDT-HG Data - Phase B* Hover – Thrust, Torque, FM vs RPM.

Phase B* Rotor Thrust & Torque Comparisons

In this section, the RotCFD vs. TDT-HG comparisons are presented as individual upper/lower rotor thrust and upper/lower rotor torque (i.e. 4 charts per figure) plotted versus rotor speed (RPM) for given shaft angle (SA) and

tunnel speed (V). Note that comparisons in this section are intentionally not presented as combined coaxial rotor thrust/power due to the objective of understanding the predictive capability of RotCFD with respect to individual rotor performance and rotor-rotor interactional aerodynamics.

The comparisons in Figs. 17-24 include figure captions with information about relevancy to Mobility CLS flight conditions (i.e. take-off climb, steep/shallow climb, scout, fast cruise, descent, landing, VRS). This means that at least one rotor (typically >= 600 RPM) in the figure is relevant to the respective condition. The designation VRS (vortex ring state) includes TWS (turbulent wake state) and is assigned to a figure when a curvature change is observed in the thrust vs. torque data. Some expected trends in rotor-rotor interactional aerodynamics are: As the rotors are separated by D/4, upper/lower rotor interaction in climb and edgewise scout/cruise flight (and conversely lower/upper interaction in steep descent) is expected to be small at lower rpm (i.e. low thrust) and as the tunnel speed V increases. More precisely, the upper rotor wake is expected to not interact with the lower rotor, if the upper rotor wake does not get ingested into the lower-rotor inflow, but actually convects downstream at some distance above the lower rotor.

In these cases, both rotors practically operate as single isolated rotors w/o interactional aerodynamics effects at similar thrust and torque. As the rotor downwash is proportional to the square-root of thrust (which itself is proportional to RPM^2), one can expect weak upper/lower interactional effects at low RPM, and gradually also for higher RPM with increasing tunnel speed V (as the upper rotor wake gets 'washed away' quickly). In addition, the effect of 'wake clearance' is expected to occur earliest in more edgewise (i.e. scout and cruise) conditions for -15deg < SA < +15deg. Indeed, classical scaling of the so-called wake skew angle versus rotor advance ratio (with individual rotor thrust coefficient C_T as a parameter) has been taken into account when designing the Phase B* rotor as a Dragonfly candidate rotor. In this context, the effects of rotor-rotor interactional aerodynamics are important with respect to the predictive capability of RotCFD for relevant flight conditions, as is discussed further below.

Of note is also that the TDT test speed of V = 6m/s was the lowest tunnel speed that could be maintained steady in the TDT (turbulence level unknown). This means that V = 2.25m/s, 4.5m/s data were taken during 'coasting-down' of the TDT. It was determined that tunnel coasting-down occurred at a much slower rate than to notably have affected 2s-5s data recording. In the following, some general observations are discussed with respect to RotCFD versus TDT-HG comparisons in Figs. 17-24.

For take-off climb in Fig. 17, Both thrust and torque comparisons are very good across all rotor RPM. Torque in particular is predicted very well. The data uncertainty for thrust are quite large, which was driven by the load-cell sensitivity at low tunnel speed and out-of-run repeatability. For the steep climb case in Fig. 18, rotor performance predictions are quite good and within data bounds for both thrust versus RPM and torque versus thrust. In general, rotor torque is predicted very well (i.e. within a few percent). Moving towards a shallower climb at SA=-30deg at the same tunnel speed of V=6m/s in Fig. 19, a different observation can be made. From a TDT-HG data standpoint, the observation is that measured TDT-HG thrust data (for the upper rotor) are getting closer to measured lower rotor thrust, which suggests that the measured TDT-HG data do exhibit less rotor-rotor interaction than predicted by RotCFD, which now tends to over-predict rotor thrust. This is also reflected in the corresponding torque/power versus thrust plots, with rotor torque values being better predicted than rotor thrust.

For scout and cruise conditions in Figs. 20-21, the previous observations concerning rotor-rotor interaction are notably less pronounced at a shaft angle of SA=-15deg. This is attributed to lower rotor-rotor interactional aerodynamics effects at lower shaft angle where now the tunnel speed V has its largest effect on convecting the upper rotor wake away from interacting with the lower rotor. Indeed, the over-prediction of upper rotor thrust at high RPM is less pronounced. Figure 21 reports a fast cruise-type condition at V=9m/s. Here RotCFD predicts rotor thrust within the experimental uncertainty bars for all conditions. For most RPMs, the predictions coincide with the experimental TDT-HG measurements. The torque comparisons in Fig. 21 again show good agreement with all conditions appearing to be mostly within the experimental uncertainty bars.

A typical descent case is shown in Fig. 22. Here the first notable observation is that the lower rotor thrust (red) is higher than that of the upper rotor thrust (black) up to the cross-over point at 900 RPM where the downwash generated by the upper rotor is strong enough to reverse the thrust contributions. It is notable that RotCFD and its actuator-disk concept can capture this complex interaction very well. Indeed free-wake analyses conducted by Dragonfly team members revealed significant challenges with wake instability in this complex rotor-rotor interaction problem; also, fully blade-resolved CFD simulations showed difficulties in converging the solution. Even though only steady-state solutions are sought using RotCFD, mean values compare very well to measured TDT-HG data for both rotor thrust and torque. Altogether, this sample complex descent condition provided high confidence to the Dragonfly team of using an efficient actuator-disk URANS model (such as RotCFD) for mean rotor performance predictions.

As far as an actual landing case in Fig. 23 is concerned, RotCFD predictions are very good (similar to the take-of climb in Fig. 17). Here the RotCFD predictions are observed to fall within the experimental uncertainty bars. At the lowest RPM, upper and lower rotor thrust are almost equal because of the axial descent velocity pushing upwards through the rotors, thereby affecting upper/lower rotor interaction. As the

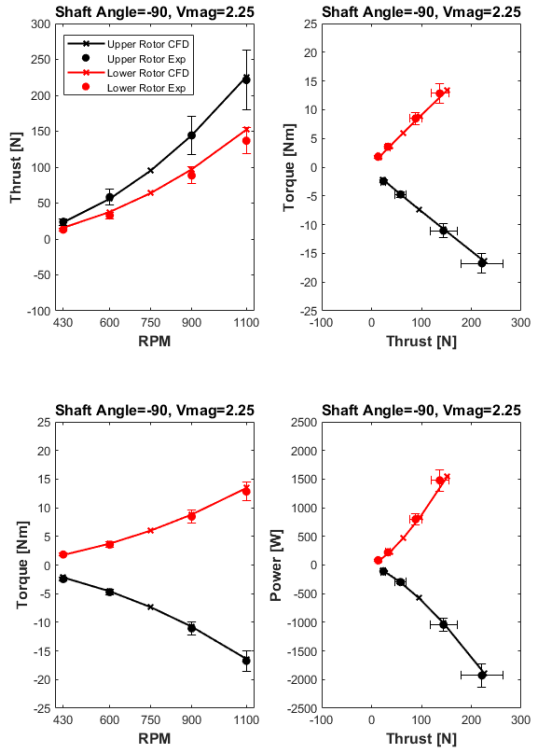

Figure 17. Take-Off Climb (SA = -90deg, V = 2.25m/s).

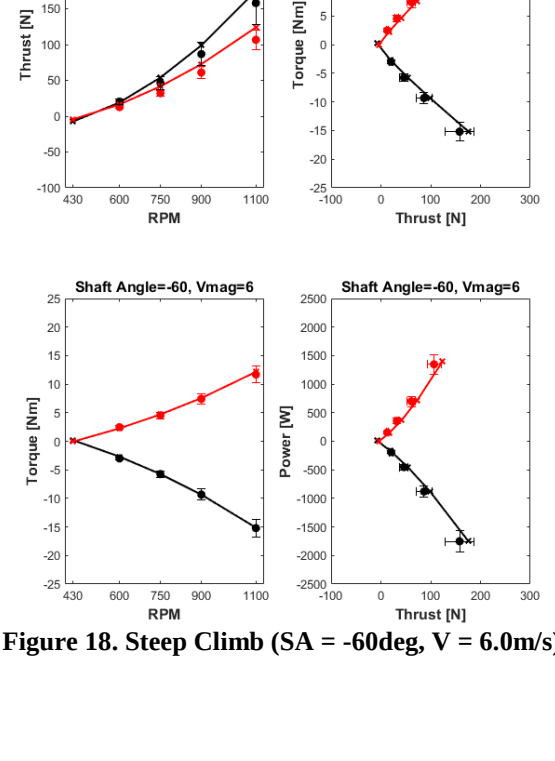

Figure 18. Steep Climb (SA = -60deg, V = 6.0m/s).

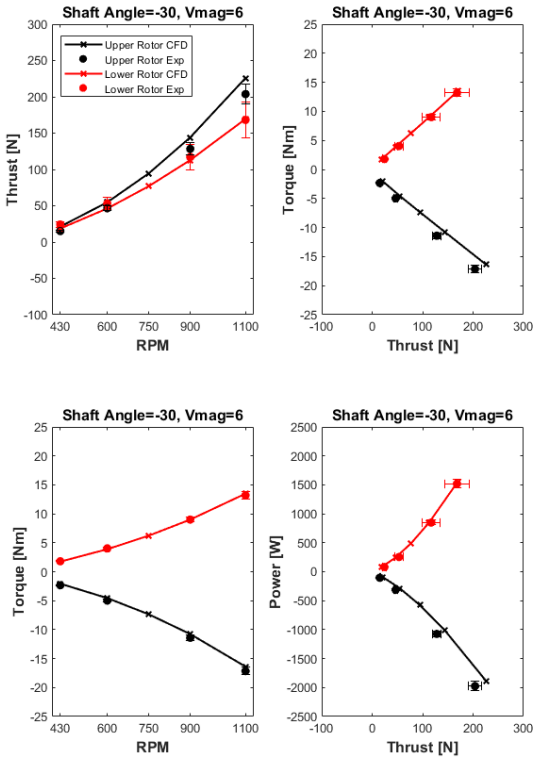

Figure 19. Climb (SA = -30deg, V = 6.0m/s).

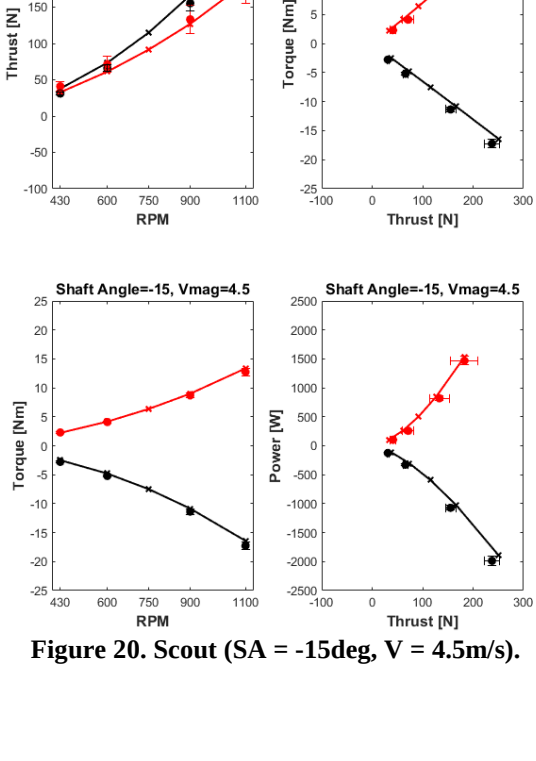

Figure 20. Scout (SA = -15deg, V = 4.5m/s).

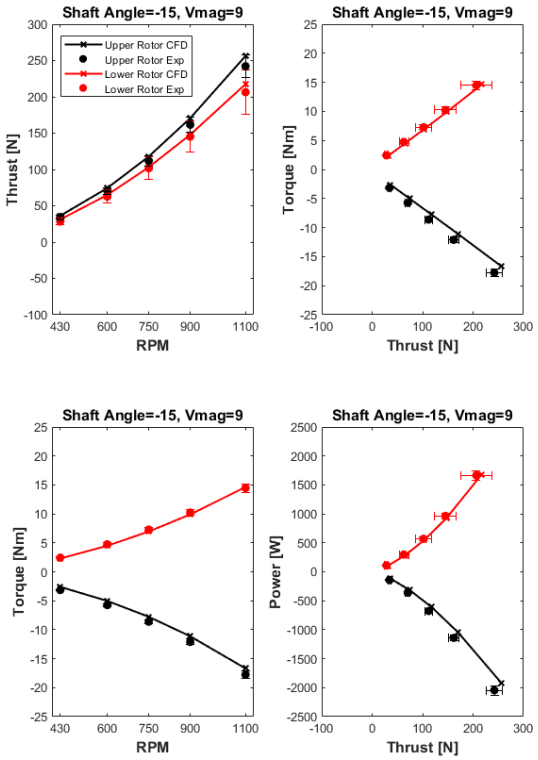

Figure 21. Fast Cruise (SA = -15deg, V = 9.0m/s).

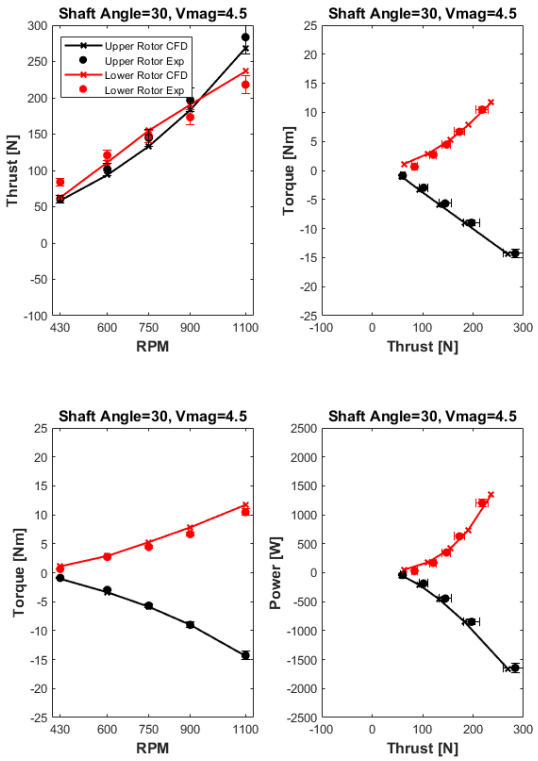

Figure 22. Descent (SA = +30deg, V = 4.5m/s).

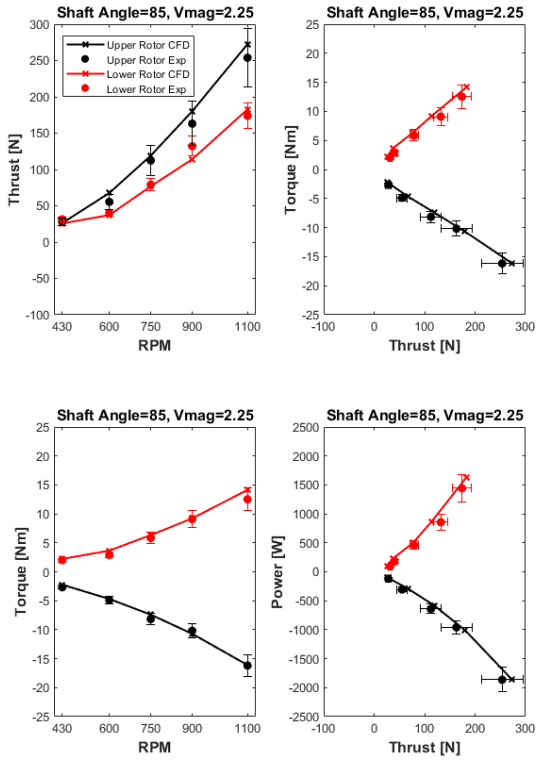

Figure 23. Landing (SA = +85deg, V = 2.25m/s).

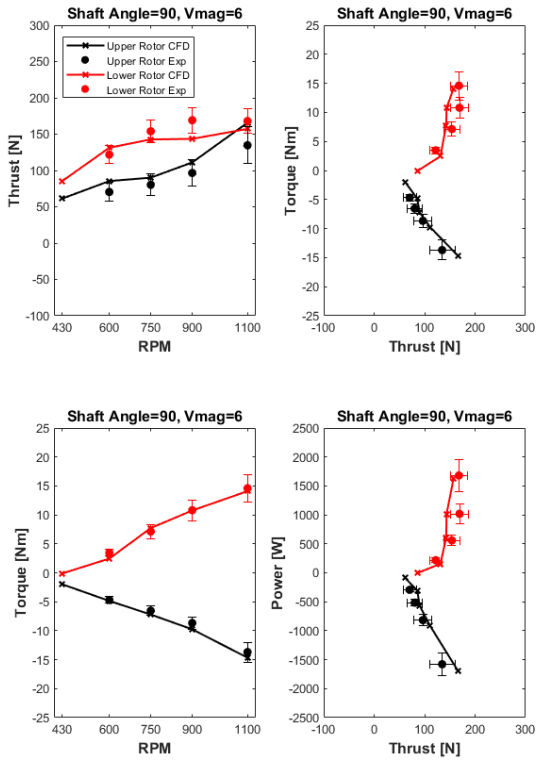

Figure 24. VRS (SA = +90deg, V = 6.0m/s).

RPM increases, the upper rotor thrust increases above that of the lower rotor, as expected. Throughout all conditions, both rotor thrust and torque are predicted within the experimental uncertainty bars.

Last but not least, a sample VRS condition in steep axial descent is shown in Fig. 24. It is noteworthy though that RotCFD still captures the overall behavior seen, for example, in curvature changes of thrust versus RPM/torque plots. The first points at 430 RPM show a near-zero torque for the lower rotor, indicating near WBS conditions. For all RPM values, the lower rotor thrust (red) is higher than that of the upper rotor (black), as expected in this steep descent condition. As the rotor speed increases, a driving torque is quickly required on the lower rotor indicating its exit from WBS towards VRS. At the higher RPM values, there are clear inflection points in the rotor thrust and torque plots, which were confirmed with flow visualization as VRS-type cases with high thrust fluctuations (up to 30%) in the measured values, not accounted for in the experimental uncertainties. Besides the fact that these VRS-type conditions are outside the steady-state rotor flight regime due to dynamic thrust fluctuations associated with this rotor state, it is impressive to see that RotCFD predicts the trends quite well considering this challenging condition.

In summary, it is very interesting to see that RotCFD with its actuator-disk URANS implementation does capture all thrust/torque trends compared to mean TDT-HG data, albeit the complexity of the aerodynamic interactions.

Phase B* Rotor Performance Coefficients Comparisons

This section discusses comparisons between computed RotCFD and measured TDT-HG rotor performance data for a different selection of the data presented in the previous section. Here comparisons are presented for dimensionless performance coefficients C_T and C_Q of the combined upper/lower coaxial system, with the objective of evaluating the overall RotCFD predictive capability over a full range in shaft angles at a given speed and selected rotor RPM.

Even though the focus is on direct rotor performance comparisons in TDT-HG, results obtained with RotCFD at Titan conditions are also included to demonstrate that the scaling difference between TDT-HG and Titan conditions is smaller than the difference between RotCFD (in HG) versus measured TDT-HG data. This provided further support that the Phase B* rotor was well designed for Re scaling between TDT-HG and Titan conditions. The comparisons are shown in Fig. 25 and are presented consistent with those shown for the TDT-HG to Titan scaling in an earlier section (see Fig. 12). Here in Fig. 25, measured TDT-HG data are plotted in 'blue', with error bars both for C_T and C_Q; computed RotCFD results are plotted in 'red' (TDT-HG) and 'black' (Titan). Therefore, the primary comparisons are 'blue' vs. 'red' in the respective figures. The comparisons are conducted exclusively at 600 and 900 RPM as these are a) representative of other rotor speeds, and b) correspond to an average rotor speed in descent (600 RPM) and scout/cruise (900 RPM).

In general, the middle plot C_T vs. μ_x is quite informative as it shows both the range in C_T between axial climb and descent along with the maximum edgewise advance ratio μ_x. Consequently, the 900 RPM case shows the inner polar curve of lower C_T range and lowest μ_x max. Furthermore, the TDT-HG data uncertainty in C_T increases with increasing shaft angle, particularly for the descent cases with SA > +15deg. This has been attributed to increasing dynamic loads with parts of the rotor disk experiencing beginning VRS-type conditions. Also visible in Fig. 25 is the smaller SA range of the data corresponding to the test matrix. The left plots of C_Q vs. C_T are also informative in the sense that data for all tunnel speeds collapse on the left branch, while the right branches differentiate based on the shaft angle at which the rotor system enters VRS.

Here it is again visible that TDT-HG data uncertainty also increases. The right plots of C_Q vs. μ_x are insightful with respect to the range in torque coefficient, with some computed RotCFD cases in WBS ($C_Q < 0$, not relevant for the flight envelope).

In summary, comparisons of RotCFD computed rotor performance against measured TDT-HG data are favorable over all tested shaft angles, ranging from axial climb to edgewise flight and steep descent. TDT-HG data uncertainty increases in descent conditions due to complex flow interactions. It was concluded that differences between rotor performance in the TDT and at Titan are notably smaller than quantitative comparisons of computed versus measured conditions in TDT-HG. This not only supports the robustness in Reynolds scaling of rotor aerodynamics, but also lets the Dragonfly Mobility team drive its uncertainty in rotor tables by the TDT comparisons, see next section.

UNCERTAINTY QUANTIFICATION FOR MOBILITY CLS

Quantitative comparisons between predicted RotCFD rotor performance and measured TDT-HG data were very good for the simulation fidelity used. The comparisons were performed over the entire experimental test matrix and included all conditions that data were obtained for in a steady-state manner. Shaft angles reported include: -90, -85, -75, -60, -45, -30, -15, -5, 0, 5, 15, 30, 45, 60, 75, 85, and 90 degrees. Flight speeds reported include: 2.25, 4.5, 6, 7.5, 9, 10.5, and 12 m/s wind tunnel speeds. The RPM for each condition was swept across 430, 600, 750, 900, and 1100 RPM.

Test Comparisons (RotCFD vs. TDT-HG) - Average

The next set of plots in Fig. 26 show the percent delta between the CFD predictions and experimental measurements at each test condition as displayed on a rotor aerodynamic state chart.

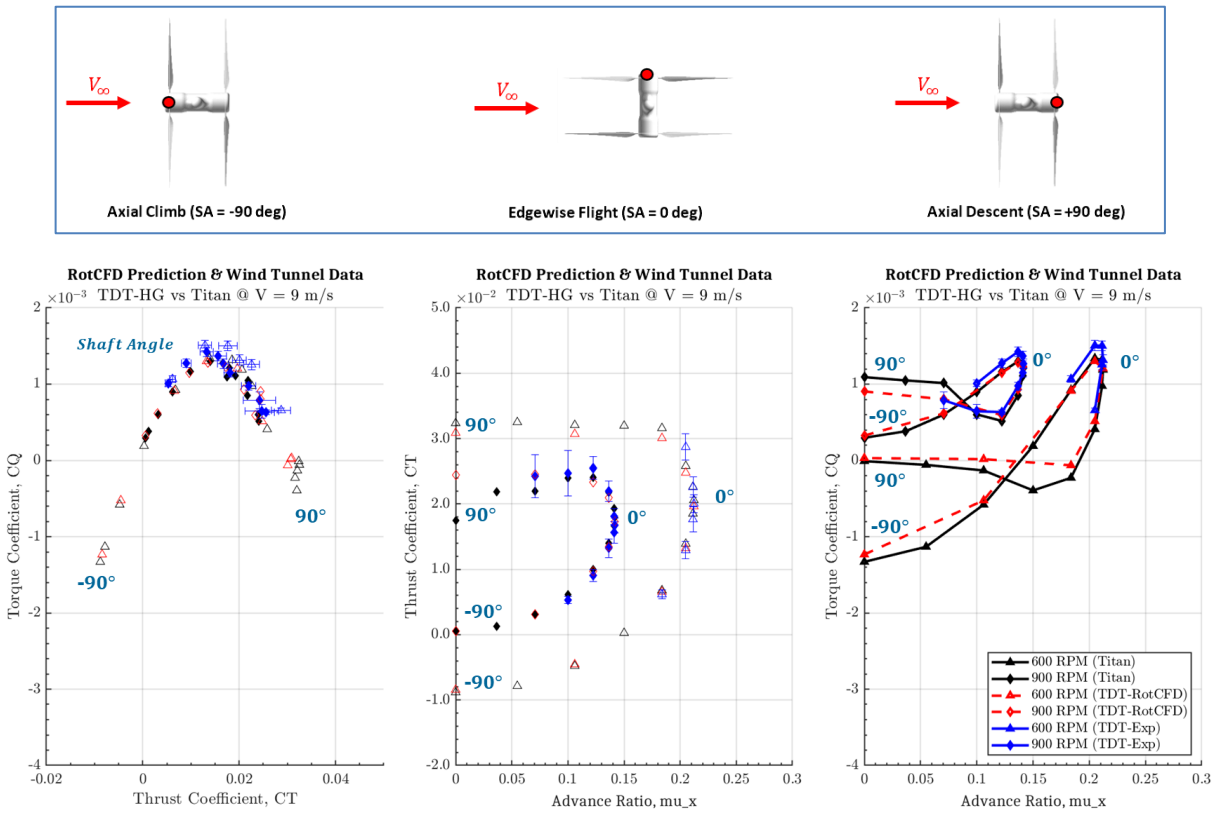

Figure 25. RotCFD – Titan vs TDT-HG (Full SA range, CRUISE speed, V = 9.0m/s).

Shaft Angles: -90,-85,-75,-60,-45,-30,-15,-5,0,+5,+15,+30,+45,+60,+75,+85,+90deg

These are shown as coaxial rotor metrics for both coaxial thrust and torque. The percentage discrepancy is reported as 100*(CFD – EXP)/EXP.

In particular, the plots shown in Fig. 26 contain the RotCFD rotor performance look-up table comparisons against measured TDT-HG data discretized by flight condition. The flight envelope is first reduced from a three-dimensional representation of rotor shaft angle, flight speed, and RPM to the reduced-order latent space defined by the vertical and horizontal speed parameters. The speed parameters are non-dimensionalized by the equivalent hover induced inflow velocity following the approach described by Marshall et al. (Ref. 17). The predicted coaxial rotor thrust for each condition is used to place each condition on the rotor state charts.

This discretizes the flight envelope into four major flight regimes: 1) steep climb, 2) shallow climb including edgewise flight, 3) shallow descent, and 4) steep descent. Here the boundary between steep and shallow climb was set at 40 degrees rotor shaft angle to the freestream flow. Within each of the flight regimes, radial bands (at constant shaft angle) are used to further discretize the rotor performance lookup table uncertainty into zones, shown as concentric rings in Fig. 26. For the same RPM, a higher zone represents a higher flight speed. Due to the nature of the non-dimensionalization by the equivalent induced hover velocity, however, the relevant flight velocities cannot be directly tied to the individual zones. For example, a low RPM and low flight speed case could be in the same zone as a higher RPM condition with a higher flight speed. As a general rule of thumb though, points closer to the origin of the graph are closer to a hover condition than those farther from the origin which would have either a high advance ratio (for edgewise flight) or high inflow ratio (for axial climb). Finally, a vortex ring state (VRS) zone was defined with a simplified rectangular boundary starting at Vz/vh = -0.45 and from axial descent through a Vx/vh of 0.5. Data falling within this VRS zone are only used to calculate the VRS zone uncertainty and were removed from the steep descent uncertainty calculations. Outliers were removed using the MATLAB function ‘rmoutliers’ with a mean filter. Using this function, outliers are defined as elements more than three standard deviations from the mean. The filter removed about 5% of the original 367 test conditions. There was no observed pattern in the conditions removed. Therefore, the outliers were assumed to arise either from issues with a particular RotCFD simulation or challenges in obtaining the data during the experiment.

Figure 26 illustrates that RotCFD predictions are within +/- 5 to 10% at typical flight conditions over the flight envelope for both coaxial rotor thrust and torque. Some larger discrepancies are seen for rotor thrust in steep climb and rotor torque in VRS (both outside the typical flight envelope). Table 2 presents average delta thrust and torque for both upper and lower rotors as well as corresponding root-mean square deviation (RMSE) over all points presented in Fig. 26. Though not being used as such in Mobility CLS, data presented in Table 2 give a general sense of the overall quality of the comparisons.

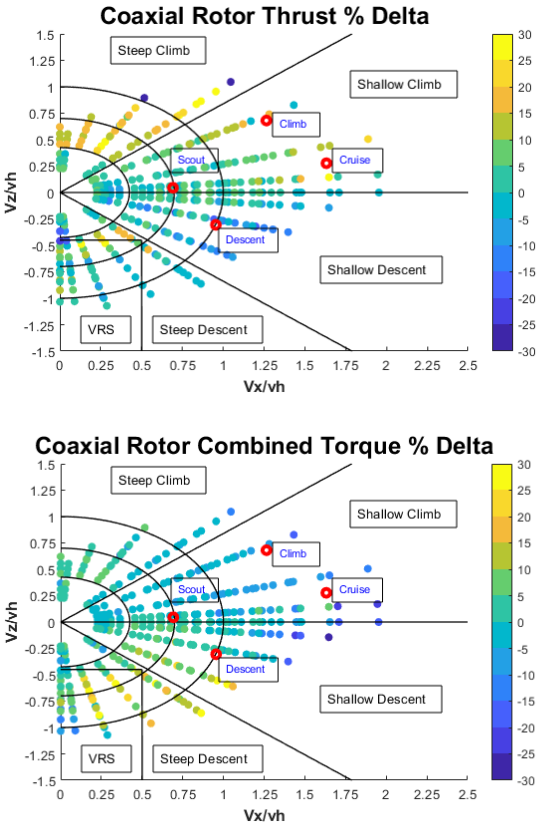

Figure 26. Coaxial Rotor Thrust/Torque Delta [%]. (RotCFD vs. TDT-HG)

Table 2. RotCFD vs. TDT-HG Data Comparisons.

	Upper Thrust [N]	Upper Torque [Nm]	Lower Thrust [N]	Lower Torque [Nm]
Avg. Δ	7.24%	-0.88%	0.45%	4.52%
Avg. Δ	6.31 N	0.02 Nm	-.1.32 N	0.28 Nm
RMSE	17.58 N	0.80 Nm	18.32 N	0.83 Nm

Test Comparisons (RotCFD vs. TDT-HG) - Histograms

The objective is to provide the Dragonfly Mobility team with uncertainty levels (of specified confidence level) for their Monte-Carlo simulations on Titan. There are a few important aspects that have to be kept in mind when defining an overall uncertainty for Mobility CLS at Titan conditions based on the TDT experiment of an isolated coaxial rotor experiment in TDT-HG at one-third scale Reynolds number compared to Titan: i) Mobility bases all their predictions on CFD tables at Titan conditions (not on TDT-HG data or any other experimental data); hence the primary objective for TDT-HG testing is not to generate tables for Mobility CLS, but to determine the validation error of the CFD TDT-HG tables over specific regions of the Dragonfly flight regime. Therefore, actual measured data uncertainty are to play an indirect role in the uncertainty provided to Mobility CLS, but they nonetheless do assist in quantifying the validation uncertainty of CFD TDT-HG tables; ii) some uncertainty may (or may not) have to be considered when scaling CFD tables from TDT-HG to Titan conditions, depending on whether or not the validation error is larger than the scaling step from TDT-HG to Titan; iii) uncertainty associated with fore/aft rotor interaction as well as rotor-body interaction is not part of the uncertainty quantification in this paper but it is currently being conducted separately for design and analysis of an anticipated second TDT experiment of a half-scale Dragonfly lander.

Therefore, four types of uncertainty are of concern in this paper: 1) Experimental data uncertainty, 2) Total CFD modeling uncertainty, 3) Validation error uncertainty, and 4) TDT => Titan scaling uncertainty. Here 1) to 3) are not separate but interconnected. If e.g. experimental data and CFD uncertainty are notably smaller than the validation error uncertainty (i.e. the difference between CFD and experimental data, here assuming that the experiment defines the truth value), then the overall uncertainty is driven by the validation error uncertainty itself; however, if all 1) to 3) i.e. experimental, CFD, and validation error uncertainty are either close to one another or the validation error uncertainty is even smaller than the experimental and CFD uncertainties, then the overlap can also be seen as a confidence level in that the actual truth value is within that range and not, for example, in opposite trend to the validation uncertainty.

In order to safely use predictions of CFD in assessment of flight dynamics and performance, it is necessary to place boundaries around the nominal predictions which contain the (unknown) true results with specified confidence. Insight into these bounds is gained by finding bounds which contain a specified fraction of all TDT-HG wind tunnel test results. This could be done with a simple scale factor (for example +/- 10%), but that can be over-conservative due to the high relative uncertainty of small-magnitude predictions. Instead, it was found that a linear bound of the form (absolute uncertainty + relative uncertainty) times CFD prediction was a better definition. This is not uniquely defined for a given confidence level, so the selected bound is that for which the samples outside the confidence limit are not correlated to CFD prediction magnitude, and therefore the error is not dominated by either the high or low magnitude values.

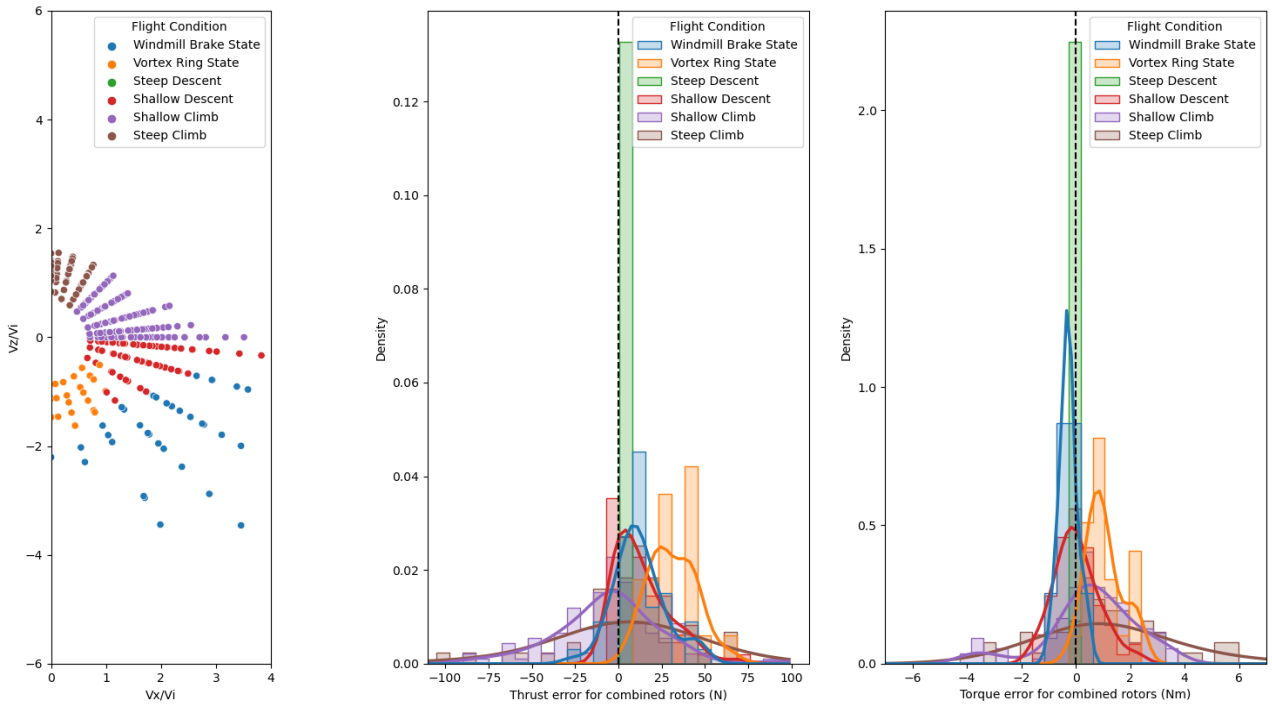

Figure 27. Histograms of RotCFD vs. mean TDT-HG data (Full Test Matrix).

Figure 27 shows histograms of CFD thrust/torque error compared to TDT-HG data based on subdividing the flight regime according to Fig. 26. This provides a visual representation of the comparisons in the various flight regimes. It can be seen that descent has in general more concentrated histogram distributions than climb (particularly steep climb). This is consistent with quantitative comparisons discussed earlier.

For the RotCFD results versus TDT-HG data comparisons altogether, Table 3 shows the 95% bound in per-rotor thrust to be +/- (10 N + 15%) and for torque +/- (1 Nm + 10%). For a 90% bound, for example, this reduces slightly to per-rotor thrust of +/- (8N + 12%) and for torque +/- (0.6Nm + 7%). The RotCFD prediction error is not quite the same across the entire flight envelope; therefore, Table 3 also displays 95% bounds for subsets of the TDT-HG data corresponding to partitions of the flight envelope such as steep climb, shallow descent, etc. Here it becomes apparent that both shallow climb and descent have lower bounds, while steep climb analyzed on its own (with limited samples) has notably higher bounds.

Overall, it is concluded that the stated 'All data' bounds (95% confidence, i.e. 2σ) for torque of +/- (1 Nm + 10%) are very reasonable, and the corresponding thrust uncertainty of +/- (10 N + 15%) has a relative uncertainty that is perhaps higher than desired, which is driven by particular rotor-rotor interaction in steep climb at the edge of the nominal flight envelope. It is noteworthy that the stated uncertainties do assume that the TDT-HG measurements are indeed the truth data. Here arguments can be brought forward in favor and opposed to this assumption.

Table 3. RotCFD vs. TDT-HG.
(Absolute + Relative Uncertainty)

Flight Regime	Coax Thrust	Coax Torque
All Data (90% bound)	**± (8N + 12%)**	**± (0.6Nm + 7%)**
All Data (95% bound)	**± (10N + 15%)**	**± (1Nm + 10%)**
Shallow Climb (95%)	± (10N + 12%)	± (1.5Nm + 3%)
Steep Climb (95%)	± (20N + 25%)	± (0.3Nm + 35%)
Descent (95%)	± (10N + 10%)	± (0.6Nm + 4%)
VRS (95%)	± (6N + 15%)	± (0.5Nm + 5%)
WBS (95%)	± (12N + 14%)	± (0.5Nm + 6%)

In fact, data uncertainty and consistency between Re-scaling measurements in TDT-Air vs TDT-HG do support this notion. At the same time, it does not seem justifiable adding additional CFD uncertainties to those stated above. On the contrary, the RotCFD grids presented earlier in this paper can be considered final within a percent of performance coefficients. Furthermore, the scaling behavior of the Phase B* rotor from TDT-HG to the Titan environment proved no significant change in rotor behavior that would have to be

accounted for with a separate uncertainty. The remaining RotCFD uncertainties concern the C81 tables that were computed with state-of-the-art OVERFLOW (SA turbulence model). Here an independent C81 table generation by another partner and using a different turbulence model may be warranted in a future investigation.

In summary, the TDT experiment has provided valuable experimental data in HG on the Phase B* coaxial rotor system that were compared to RotCFD rotor performance predictions. Furthermore, the Reynolds scaling behavior of the Phase B* rotor from TDT-Air to TDT-HG supports that consistent performance is expected for the current Phase C rotor configuration. Based on the various analyses conducted in this paper, it was recommended that Mobility CLS use the above stated validation uncertainty bounds (95% confidence, 2σ) of +/- (10 N + 15%) for thrust and +/- (1 Nm + 10%) for torque in their continued simulations. In addition, it was suggested that the Dragonfly Mobility team explore the approach of using zones on the rotor state chart for varying uncertainty, accounting for adequate curvature corrections between various flight regime (or zones). The advantage of such an approach may be that uncertainties can be reduced based on specific regions of the flight envelope where the vehicle is mostly operating as actual scout, cruise, shallow climb, and landing conditions were predicted very well.

This work was important in qualifying a hybrid actuator-disk BEMT/URANS method as a predictive tool to generate rotor performance tables for use in Dragonfly Mobility CLS. It gave further rise to subsequent high-fidelity blade-resolved CFD (OVERFLOW, STAR-CCM+) within the Dragonfly program, see Refs. 32-34.

CONCLUSIONS

The fixed-pitch speed-controlled Dragonfly Phase B* rotor was tested in the NASA Langley Transonic Dynamics Tunnel (TDT). This was the first performance test of a candidate flight rotor system for NASA's Dragonfly mission in a test fluid with good dynamic similitude enabled by heavy gas in the TDT, providing Mach scaled data at one-third chord-based Reynolds number when compared to conditions expected at Titan. The present work provides a thorough CFD validation study of coaxial rotor performance estimation with accuracy of order 5-10% over the primary flight envelope using an efficient hybrid BEMT-URANS flow solver, RotCFD. The primary objective of the present work was to quantify the predictive capability of RotCFD rotor performance tables from both a validation standpoint in TDT-HG, as well as with respect to suitable uncertainties for Mobility CLS at Titan conditions.

In this context, it has to be kept in mind that validation is not the same as uncertainty. Indeed, it became apparent in the analyses presented in this paper that while validation of RotCFD versus measured TDT-HG data was very good for particular regions of the flight envelope, it varies between broad partitions of climb/descent and edgewise flight. These observations made defining an overall uncertainty for Mobility CLS a formidable task. Indeed, computing a 95% confidence (i.e. 2σ) level of all relevant TDT-HG data (weighted equally) resulted in suggested uncertainties for Mobility CLS of +/- (10N + 15%) for rotor thrust and +/- (1 Nm + 10%) for rotor torque and do not necessarily reflect the validation quality of the most relevant cases in the flight envelope. Some additional conclusions are listed below:

- The TDT test was highly valuable in assessing the predictive capability of actuator-disk BEMT/URANS CFD rotor performance tables used by Mobility CLS.
- RotCFD provides a good means of predictive capability of steady rotor performance versus computational cost, even for steep descent and VRS cases.
- Scaling TDT-HG to Titan appears straightforward with no significant change in rotor behavior. This supports that Mobility CLS can use rotor performance tables at Titan, with applied uncertainties quantified in TDT-HG.
- The Re scaling 'TDT-Air to TDT-HG' data campaign was successful and gives confidence both in data uncertainty and that a 3-bladed flight rotor with the same solidity will not experience additional Re-scaling effects.

The most important contribution of this work has been to establish the general hybrid actuator-disk BEMT/URANS method as the primary modeling tool for mean rotor performance coefficients. Since the present work has been completed, the method has been implemented to model full lander configurations and associated fore-aft rotor and rotor-body interactions on the Dragonfly lander by the full team.

Author contact: Sven Schmitz sus52@psu.edu, Jason Cornelius jason.k.cornelius@nasa.gov, Gracelyne Allred gha2@psu.edu, Jose Palacios jlp324@psu.edu, Richard R. Heisler Richard.Heisler@jhuapl.edu, Bernadine Juliano Bernadine.Juliano@jhuapl.edu, Gino Perrotta Gino.Perrotta@jhuapl.edu, Felipe Ruiz Felipe.Ruiz@jhuapl.edu.

ACKNOWLEDGMENTS

This work was funded by the NASA New Frontiers Dragonfly Mission. The authors would like to thank the NASA Langley Transonic Dynamics Tunnel staff and the larger Dragonfly experimental test team for obtaining and post-processing the experimental data. Special thanks go to Sihong Yan at Penn State for writing the control software. The authors also thank the NASA Advanced Supercomputing Division for their support in using the High-End Computing Capability Pleaides GPU nodes for this work. In addition, the authors thank Ethan Romander, Larry Young, Nicholas Peters, Sesi Kottapalli, Wayne Johnson, and Carl Russell of NASA Ames Research Center for their support. Lastly, the authors express their sincerest gratitude to Nappinai Rajagopalan and the late Dr. Ganesh Rajagopalan for the development and continued

support of the RotCFD code that has been instrumental in conducting engineering design and analysis in support of many planetary exploration studies and missions.

REFERENCES

1. Lorenz, R., Mitton, J., "Titan Unveiled," Princeton University Press, 2008. Young, L. A., "Vertical Lift - Not Just For Terrestrial Flight,"
2. Proceedings of the AHS/AIAA/RaeS/SAE International Powered Lift Conference, Arlington, VA, Oct., 2000. https://rotorcraft.arc.nasa.gov/Publications/files/Young_AHS00.pdf
3. Langelaan, J., Schmitz, S., Palacios, J., Lorenz, R., "Energetics of rotary-wing exploration of Titan," IEEE Aerospace Conference, 2704, 2017. https://doi.org/10.1109/AERO.2017.7943650.
4. Lorenz, R. D., Turtle, E. P., Barnes, J. W., Trainer, M. G., Adams, D. S., Hibbard, K. E., Sheldon, C. Z., Zacny, K., Peplowski, P. N., Lawrence, D. J., Ravine, M. A., McGee, T. G., Sotzen, K. S., MacKenzie, S. M., Langelaan, J. W., Schmitz, S., Wolfarth, L. S., and P. D. Bedini, "Dragonfly: a rotorcraft lander concept for scientific exploration at Titan," Johns Hopkins APL Technical Digest Vol. 34, No. 3, pp. 374-387, 2018. https://dragonfly.jhuapl.edu/News-and-Resources/docs/34_03-Lorenz.pdf
5. Balaram, B., Canham, T., Duncan, C., Golombek, M., Grip, H., Johnson, W., Maki, J., Quon, A., Stern, R., Zhu, D., "Mars Helicopter Technology Demonstrator," AIAA SciTech Forum, Kissimmee, FL, Jan. 2018. https://doi.org/10.2514/6.2018-0023.
6. Koning, W., Johnson, W., and Grip, H., "Improved Mars Helicopter Aerodynamic Rotor Model for Comprehensive Analyses," AIAA Journal, Vol. 57, No. 9, Sept. 2019. https://doi.org/10.2514/1.J058045.
7. Grip, H., Johnson, W., Malpica, C., Scharf, D., Mandic, M., Young, L., Allan, B., Mettler, B., San Martin, M., Lam, J., "Modeling and Identification of Hover Flight Dynamics for NASA's Mars Helicopter," AIAA Journal of Guidance, Control, and Dynamics, Vol. 43, No. 2, Feb. 2020. https://doi.org/10.2514/1.G004228.
8. Johnson, W., Withrow-Maser, S., Young, L., Malpica, C., Koning, W.J.F., Kuang, W., Fehler, M., Tuano, A., Chan, A., Datta, A., Chi, C., Lumba, R., Escobar, D., Balaram, J., Tzanetos, T., Grip, H., "Mars Science Helicopter Conceptual Design," NASA/TM–2020–220485. https://rotorcraft.arc.nasa.gov/Publications/files/MSH_WJohnson_TM2020rev.pdf
9. Balaram, J., Aung, M., Golombek, M. P., "The Ingenuity Helicopter on the Perseverance Rover," *Space Science Reviews*, Vol. 217, No. 56, 2021.
10. Escobar, D., Chopra, I., Datta, A., "High-Fidelity Aeromechanical Analysis of Coaxial Mars Helicopter," AIAA Journal of Aircraft, Vol. 58, No. 3, May 2021. https://doi.org/10.2514/1.C035895.
11. Tzanetos, T., Aung, M., Balaram, J., Grip, H., Karras, J., Canham, T., Kubiak, G., Anderson, J., Merewether, G., Starch, M., Pauken, M., Cappucci, S., Chase, M., Golombek, M., Toupet, O., Smart, M., Dawson, S., Ramirez, E., Lam, J., Stern, R., Chahat, N., Ravich, J., Hogg, R., Pipenberg, B., Keennon, M., Williford, K., "Ingenuity Mars Helicopter: From Technology Demonstration to Extraterrestrial Scout," IEEE Aerospace Conference (AERO), Big Sky, MT, 2022.
12. J.W. Barnes, E.P. Turtle, M.G. Trainer, R.D. Lorenz, S.M. MacKenzie, W.B. Brinckerhoff, M.L. Cable, C.M. Ernst, C. Freissinet, K.P. Hand, A.G. Hayes, S.M. Hurst, J.R. Johnson, E. Karkoschka, D.J. Lawrence, A. Le Gall, J.M. Lora, C.P. McKay, R.S., "Science Goals and Objectives for the Dragonfly Titan Rotorcraft Relocatable Lander," *The Planetary Science Journal*, Vol. 2, No. 18, 2021. https://doi.org/10.3847/PSJ/abfdcf
13. "Why Titan?" The Johns Hopkins University Applied Physics Laboratory. https://dragonfly.jhuapl.edu/Why-Titan/
14. Moorman, R. W., "Dragonfly Evolution," *Vertiflite*, November/December Issue, pp. 24-28, 2024.
15. NASA Langley Research Center, "Rotors for Mission to Titan Tested at Langley's Transonic Dynamics Tunnel," December 2022. https://www.nasa.gov/feature/langley/rotors-for-mission-to-titan-tested-at-langley-s-transonic-dynamics-tunnel
16. Cornelius, J., Schmitz, S., "Rotor Performance Predictions for UAM – Single vs Coaxial Rigid Rotors," The VFS Aeromechanics for Advanced Vertical Flight Technical Meeting, San Jose, CA, January 25-27, 2022. https://rotorcraft.arc.nasa.gov/Publications/files/Jason_Cornelius_Schmitz_12-Jan-22.pdf
17. Marshall, M., Tang, E., Cornelius, J., Ruiz, F., Schmitz, S., "Performance of the Dragonfly Lander's Coaxial Rotor in Vortex Ring State," AIAA SciTech Forum, AIAA 2024-0247, Miami, FL, Jan. 2024. https://doi.org/10.2514/6.2024-0247
18. Cornelius, J., Schmitz, S., Kinzel, M., "Efficient Computational Fluid Dynamics Approach for Coaxial Rotor Simulations in Hover," *AIAA Journal of Aircraft*, Vol. 58, No. 1, Jan. 2021. https://doi.org/10.2514/1.C036037
19. Kinzel, M., Cornelius, J., Schmitz, S., Palacios, J., Langelaan, J., Adams, D., Lorenz, R., "An Investigation of the Behavior of a Coaxial Rotor in Descent and Ground Effect," AIAA SciTech Forum, San Diego, CA, Jan. 7-11, 2019. https://doi.org/10.2514/6.2019-1098
20. Cornelius, J., Zhang, J., Schmitz, S., Smith, E., "Comprehensive Analysis of Coaxial Rotor Dynamics on

a Support Arm," AIAA SciTech Forum, San Diego, CA, Jan. 3-7, 2022. https://doi.org/10.2514/6.2022-0930

21. Cornelius, J., "Mid-Fidelity Performance Analysis for Fixed-Pitch Speed-Controlled Multirotor Aircraft," Dissertation in Aerospace Engineering, The Pennsylvania State University, Aug. 2023. https://etda.libraries.psu.edu/catalog/20665joc5693
22. Cornelius, J., Schmitz, S., "Coaxial Rotor CFD Validation and ML Surrogate Model Generation," VFS Aeromechanics Specialists' Conference, Santa Clara, CA, Feb. 2024.
23. Lorenz, R. D., Schmitz, S., Kinzel, M., "Prediction of Aerodynamically-triggered Condensation: Application to the Dragonfly Rotorcraft in Titan's Atmosphere," Aerospace Science and Technology, Vol. 114, July 2021. https://doi.org/10.1016/j.ast.2021.106738
24. Rajagopalan, G., Baskaran, V., Hollingsworth, A., Lestari, A., Garrick, D., Solis, E., and Hagerty, B., "RotCFD – A Tool for Aerodynamic Interference of Rotors: Validation and Capabilities," AHS Future Vertical Lift Aircraft Design Conference, San Francisco CA, Jan. 2012.
25. Sukra Helitek, RotCFD: Rotor Computational Fluid Dynamics Integrated Design Environment, Software Package, Ver. 0.9.15 Build 402, Ames, IA, 2020. http://sukra-helitek.com/
26. Conley, S., Russell C., Kallstrom K., Koning W., Romander E., "Comparing RotCFD Predictions of the Multirotor Test Bed with Experimental Results," VFS 76th Annual Forum, Oct. 2020. https://rotorcraft.arc.nasa.gov/Publications/files/1429_Conley_070720.pdf
27. Rajagopalan, G., Thistle, J., and Polzin, W., "The Potential of GPU Computing for Design in RotCFD," AHS Technical Meeting on Aeromechanics Design for Transformative Vertical Lift, San Francisco, CA, Jan. 2018.
28. Koning, W., Allan, B., Romander, E., Johnson, W., "Comparing 3D and 2D CFD for Mars Helicopter Ingenuity Rotor Performance Prediction," 49th European Rotorcraft Forum, Buckeburg, German, September 2023
29. Mathur, S. R., and Murthy, J. Y., "A Pressure-based Method for Unstructured Meshes," *Journal of Numerical Heat Transfer*, Vol. 31, No. 2, pp. 195-215. https://doi.org/10.1080/10407799708915105
30. OVERFLOW 2.3d, Overset Grid Computational Fluid Dynamics Flow Solver With Moving Body Capability (OVERFLOW), NASA Software Catalog, 2023. https://software.nasa.gov/software/LAR-20095-1
31. Spalart, P., Allmaras, S., "A One-Equation Turbulence Model for Aerodynamic Flows," AIAA 30th Aerospace Sciences Meeting and Exhibit, Jan. 1992. https://doi.org/10.2514/6.1992-439
32. Ventura Diaz, P., Yoon, S., Edquist, K., "High-Fidelity Computational Modeling of Dragonfly Lander during Preparation for Powered Flight," VFS Forum 81 Annual National Forum, May 2025.
33. Gruber, K., Regan, M., Trubelja, K., Klimchenko, V., Bowles, P., Misiorowski, M., Perrotta, G., "The Evolution of Dragonfly's Design Using CFD at Titan," VFS Forum 81 Annual National Forum, May 2025.
34. Lorber, P., Wallace, B., Sharma, K., McGrath, B., Kellermeyer, W, Edquist, K., Giels, P., Bowles, P., "Dragonfly Preparation for Powered Flight Wind Tunnel and CFD Modelling," VFS Forum 81 Annual National Forum, May 2025.